UNIVERSITY OF CALIFORNIA

Santa Barbara

EXTREME ENRICHED AND HETEROGENEOUS $^{87}SR/^{86}SR$ RATIOS RECORDED IN MAGMATIC PLAGIOCLASE FROM THE SAMOAN HOTSPOT

A Thesis submitted in partial satisfaction of the

requirements for the degree Master of Science

in Earth Science

by

Mark Alexander Edwards

Committee in charge:

Professor Matthew Jackson, Chair

Professor Roberta Rudnick

Professor Frank Spera

September 2018

The thesis of Mark Alexander Edwards is approved.

_____
Roberta Rudnick

_____
Frank Spera

_____
Matt Jackson, Committee Chair

August 2018

ACKNOWLEDGEMENTS

First and foremost I thank my committee, without whom this work would not have been possible. Thanks to Matt for helping to develop many of the ideas presented here and for encouraging me to forge on with this project even when I viewed various problems or challenges as insurmountable. Thanks to Roberta for your suggestions on ways to improve this work, and generally for your unwavering dedication to asking tough questions and accepting only top-quality science which encourages all of us to improve our work and think about it more deeply. And, thanks to Frank for many discussions on topics addressed here on which you are an expert – your advice vastly improved this thesis.

I also am indebted to the coauthors of this manuscript, who greatly assisted with this thesis; specific author contributions are as follows. I conducted the majority of the analytical and preparation work, prepared the manuscript, made the figures and tables, and developed some of the ideas presented. Matt Jackson conceived the project, assisted with analytical development and data presentation, and developed many of the ideas presented here. Andrew Kylander-Clark assisted with mass spectrometry and developed the analytical methods. Jason Harvey made a series of extremely helpful TIMS measurements. Graham Hagen-Peter helped with ICP-MS characterization of a reference material and provided a secondary plagioclase reference material. Gareth Seward assisted with electron probe microanalysis and developed the quantitative mapping technique employed here. Christy Till assisted in preparing a primary reference material. Jenna Adams helped with MELTS modeling of Samoan lavas and confirmed that some of the interpretations in the manuscript are reasonable. John Cottle and Brad Hacker developed the laser-ablation split-stream mass spectrometry facility at UCSB, and helped with thinking about the data. Frank Spera helped

to think about the geochemical data, and assisted with making interpretations that are reasonable given his deep knowledge of magma mixing, petrology, and thermodynamics.

I would like to thank the Earth Science graduate students at UCSB, who are generally incredibly helpful, supportive, positive, and constructive. Pet Food seminars were helpful when first formulating the ideas that are presented in this thesis, and informal discussions with many students were incredibly helpful. Andrew Reinhard deserves special recognition for his help thinking about isotope geochemistry and grappling with intra-lava heterogeneity.

And perhaps most importantly, I would like to thank my partner Elissa McBride, who was incredibly supportive throughout my graduate career as I struggled with technical challenges, traveled for months at a time for fieldwork and mass spectrometry, or shirked social obligations to grade papers or make a deadline.

ABSTRACT

Extreme enriched and heterogeneous $^{87}Sr/^{86}Sr$ ratios recorded in magmatic plagioclase from the Samoan hotspot

by

Mark Alexander Edwards

We report the major-element, trace-element, and $^{87}Sr/^{86}Sr$ compositions of six plagioclase crystals from two Samoan lavas with extreme EM2 isotopic compositions (ALIA-115-18 with whole-rock $^{87}Sr/^{86}Sr$ of 0.718592, and ALIA-115-21 with whole-rock $^{87}Sr/^{86}Sr$ of 0.720469). We employed laser-ablation split-stream mass spectrometry (LASS) to measure $^{87}Sr/^{86}Sr$ ratios, major-element, and trace-element concentrations in the same plagioclase crystal volume simultaneously. We find that two plagioclase crystals have extreme $^{87}Sr/^{86}Sr$ heterogeneity in excess of 5000 ppm. This range is over an order of magnitude greater than the reproducibility achieved for $^{87}Sr/^{86}Sr$ reference materials, including a homogeneous natural plagioclase crystal (± 350 ppm, 2 SD). In two of the plagioclase crystals, we identify the highest $^{87}Sr/^{86}Sr$ ratios (0.7224) ever measured in any fresh, mantle-derived ocean-island basalt (OIB) or OIB-hosted mineral phase.

When $^{87}Sr/^{86}Sr$ is plotted against Sr, the six plagioclase crystals form arrays that converge on a "common component" with a more extreme EM2 signature (i.e., with higher $^{87}Sr/^{86}Sr$) than has been previously identified in whole-rock Samoan lavas or mineral separates. We use the occurrence of olivines (mean Fo = 74.5 ± 0.8, 2 SD) in the high-$^{87}Sr/^{86}Sr$ zone of one plagioclase crystal to infer the bulk composition (Mg# = 46.8 ± 0.8, 2

SD) of the extreme EM2 magma from which the olivine and high-$^{87}Sr/^{86}Sr$ plagioclase crystallized. We argue that a relatively evolved EM2 endmember magma mixed with at least one lower-$^{87}Sr/^{86}Sr$ melt to generate the observed intra-crystal plagioclase isotopic heterogeneity.

Inferring that subducted terrigenous sediment gives rise to EM2 signatures in Samoan lavas, we estimate that the quantity of sediment necessary to generate the most-elevated $^{87}Sr/^{86}Sr$ ratios observed in the Samoan plagioclase is 7.4 ± 0.2% of the mantle source. We also estimate that sediment subduction into the mantle over geologic time has generated a sediment reservoir that constitutes 0.02% of the mantle's mass, a much lower concentration than required in the EM2 mantle source. Even if subducted sediment is concentrated in large low-shear-velocity provinces (LLSVPs) at the base of the mantle (which constitute an estimated 7.7% of the mantle's mass), only 0.25% of the LLSVPs are composed of sediment. This suggests the distribution of sediment in the mantle is heterogeneous, and the high relative abundance of sediment in the Samoan EM2 mantle is an anomalous relic of ancient subduction that has survived convective attenuation.

I. Beyond EM2: extreme enriched and heterogeneous $^{87}Sr/^{86}Sr$ ratios recorded in magmatic plagioclase from the Samoan hotspot

A. Introduction

The observation that global OIB show variations in radiogenic isotopic compositions suggests that the mantle is heterogeneous (e.g., Gast et al., 1964; Hart et al., 1973; Zindler and Hart, 1986; Hofmann, 1997; Stracke, 2012; White, 2015). OIB can be grouped into distinct end-members defined by their Sr, Nd, and Pb isotopic compositions: DMM (depleted MORB mantle), HIMU ("high μ" = high $^{238}U/^{204}Pb$), EM1 (enriched mantle I), and EM2 (enriched mantle II) (Zindler and Hart, 1986). Although it is clear that isotopic differences exist in the mantle domains that are sampled by global OIB, the origins and characteristics of the isotopic "reservoirs" in Earth's mantle remain active areas of inquiry.

Studies of mantle-derived lavas most often employ whole-rock isotopic measurements, which homogenize any potential isotopic heterogeneity among different phases or within individual minerals (or melt inclusions) in a lava. Although whole-rock analyses are useful in identifying isotopic heterogeneities in Earth's mantle at the >1 m scale (e.g., Hofmann, 1997; Stracke, 2012; White, 2015), information about possible isotopic heterogeneity within a single lava is lost (Davidson et al., 2007). In this study we focus on intra-lava isotopic heterogeneity, which can provide insight into the nature of mantle heterogeneity at the cm to mm scale.

Previous work has identified $^{87}Sr/^{86}Sr$ disequilibrium between olivine-hosted melt inclusions and their host oceanic lavas, an observation that suggests multiple isotopically distinct melt sources may contribute to a single lava (or that the assimilation of crust modifies the isotopic composition of lavas after olivine crystallization) (e.g., Jackson and

Hart, 2006; Harlou et al., 2009; Sobolev et al., 2011; Reinhard et al., 2016). Pb isotopic variability has also been observed in olivine-hosted melt inclusions in OIB (Saal et al., 2005, 1998; Sobolev et al., 2011; Yurimoto et al., 2004), although the magnitude of Pb isotopic heterogeneity in inclusions has been debated (Paul et al., 2011). Furthermore, the Sr, Nd, Hf, and Pb isotopic compositions of clinopyroxene hosted in OIB lavas have been demonstrated to be in isotopic disequilibrium with their host whole rocks (Hanyu et al., 2011; Hanyu and Nakamura, 2000; Jackson et al., 2009; Miyazaki et al., 2018). Collectively, these studies suggest that intra-lava isotopic heterogeneity can be recorded in OIB. However, the mechanisms for generating this heterogeneity remain unresolved.

Plagioclase is well suited to evaluating the nature and origin of $^{87}Sr/^{86}Sr$ heterogeneity in OIB lavas because i) Sr is compatible in plagioclase, so plagioclase has elevated Sr concentrations relative to the bulk rock; ii) plagioclase has low Rb concentrations, thereby minimizing the impact of the isobaric interference of ^{87}Rb on mass 87 when employing in situ analytical methods; iii) plagioclase can contain domains (or zones) with distinct $^{87}Sr/^{86}Sr$ compositions (e.g., Christensen et al., 1995; Davidson et al., 2001; Davidson and Tepley, 1997; Font et al., 2008; Lange et al., 2013; Ramos et al., 2005); and iv) $^{87}Sr/^{86}Sr$ compositions can be linked to the major- and trace-element compositions of the plagioclase domains. Such domains record a "crystal stratigraphy" that can provide relative temporal information (from plagioclase core to rim) about the processes that contributed to the isotopic composition of a single plagioclase crystal.

To our knowledge, intra-crystal $^{87}Sr/^{86}Sr$ zonation has never been reported in plagioclase in OIB. Therefore, this study uses LASS (laser-ablation split-stream mass spectrometry; Kylander-Clark et al., 2013) to measure the $^{87}Sr/^{86}Sr$ and major- and trace-element compositions of six plagioclase crystals hosted in two extreme EM2 lavas from the Samoan

hotspot with the most elevated $^{87}Sr/^{86}Sr$ signatures ever reported in global OIB (with whole-rock $^{87}Sr/^{86}Sr$ of 0.718592 and 0.720469; Jackson et al., 2007).

B. Sample description and methods

1. Sample description and EPMA analysis

We target two lavas from the Samoan hotspot—ALIA-115-18 and ALIA-115-21—that have previously been characterized for whole-rock isotopic, major-element, and trace-element geochemistry. ALIA-115-18 and ALIA-115-21—a trachybasalt and trachyandesite, respectively—were dredged aboard the R/V Kilo Moana in April 2005 from the deep (3220 m below sea level) southwest flank of Savai'i Island, western Samoa (Figure 1) (Jackson et al., 2007; Koppers et al., 2011, 2008).

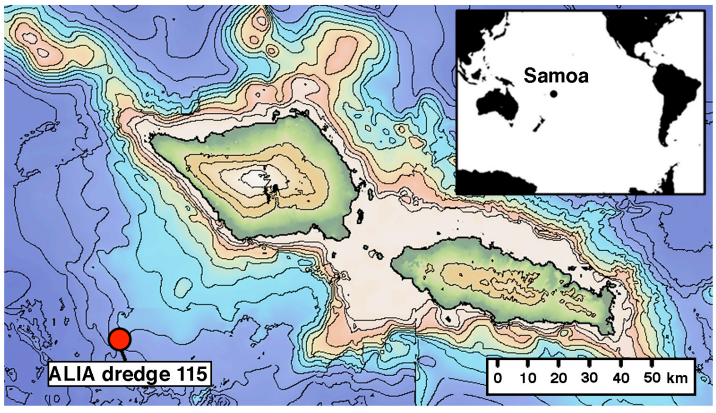

Figure 1. Map of western Samoa showing the islands of Savai'i (left) and Upolu (right). The inset shows the location of the Samoan chain in the western Pacific. The location of ALIA dredge 115 is indicated (the dredge location is from Jackson et al., 2007). The map was made with GeoMapApp using the GMRT 3.5 DEM. The contour interval is 200 m, and the contour corresponding to an elevation of 0 m is bolded.

A suite of five rocks from ALIA dredge 115 range in age from 4.98 to 5.06 Ma (Koppers et al., 2008, 2011). ALIA-115-18 (whole-rock $^{87}Sr/^{86}Sr$ is 0.718592) and ALIA-115-21 (whole-rock $^{87}Sr/^{86}Sr$ is 0.720469; Jackson et al., 2007) have the most geochemically enriched $^{87}Sr/^{86}Sr$ signatures measured in whole-rock OIB to date (Figure 2). Previous work on samples ALIA-115-18 and ALIA-115-21 also revealed significant $^{87}Sr/^{86}Sr$ disequilibrium (up to 3115 ppm and 1611 ppm, respectively) between clinopyroxene and the host whole rocks (Jackson et al., 2009), making these two samples ideal targets for investigating $^{87}Sr/^{86}Sr$ heterogeneity in OIB-hosted plagioclase. ALIA-115-18 and ALIA-115-21 host large, mm-scale plagioclase crystals (see electron probe microanalysis [EPMA] images in Supplementary Figure 1) that were targeted here. See the Supplementary Methods for a description of sample preparation, EPMA mapping of the plagioclase crystals, and EPMA analysis of olivine inclusions in plagioclase ALIA-115-18-1 (Table 1).

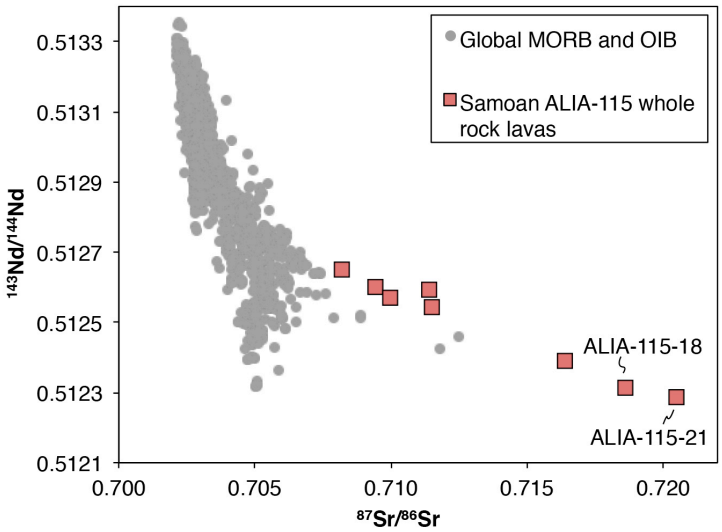

Figure 2. Global ocean island basalt and mid-ocean ridge basalt isotopic array ("mantle array") in $^{143}Nd/^{144}Nd$-$^{87}Sr/^{86}Sr$ space. Data are from the compilation of Stracke et al. (2003), with additional Samoan isotopic data from Workman et al. (2004) and Jackson et al. (2007). ALIA dredge 115 lavas are shown in red, with ALIA-115-18 and ALIA-115-21 whole rocks annotated. We investigate the compositions of plagioclase from these two whole rock lavas in this study.

2. Laser ablation split-stream mass spectrometry

We employ LASS (laser ablation split-stream mass spectrometry ; Kylander-Clark et al., 2013) to measure major- and trace-element concentrations and $^{87}Sr/^{86}Sr$ compositions simultaneously in Samoan plagioclase. This analytical approach couples a Teledyne CETAC Photon Machines *Analyte* 193 nm ArF excimer laser and HelEx sample cell to two mass spectrometers: a Nu Instruments *Plasma HR* multi-collector inductively coupled plasma mass spectrometer (MC-ICP-MS) for $^{87}Sr/^{86}Sr$ measurements, and an Agilent *7700X* quadrupole inductively coupled plasma mass spectrometer (Q-ICP-MS) for trace-element concentration measurements. The ablated sample is mixed in a mixing bulb; the sample flow path is then split so that approximately half of the sample is directed to each mass spectrometer. The LASS methods employed at UCSB (University of California at Santa Barbara) are described in detail by Kylander-Clark et al. (2013).

LASS enables investigation of the relationships between $^{87}Sr/^{86}Sr$ and plagioclase major- and trace-element geochemistry from the same laser spot, and thereby facilitates the interpretation of isotopic data. Additionally, LASS allows filtering or discarding of $^{87}Sr/^{86}Sr$ analyses that contain inclusions or other phases. As a result, LASS allows targeting of phase-specific $^{87}Sr/^{86}Sr$ data by identifying and discarding isotopic data associated with non-plagioclase trace-element signatures (Figure 3). For each ALIA-115 plagioclase crystal, a model $^{87}Sr/^{86}Sr$ and Sr concentration surface was generated from the $^{87}Sr/^{86}Sr$ and Sr concentration values and the laser spot locations using the Matlab® function ‘gridfit’ (Figure 4 and Supplementary Figure 2).

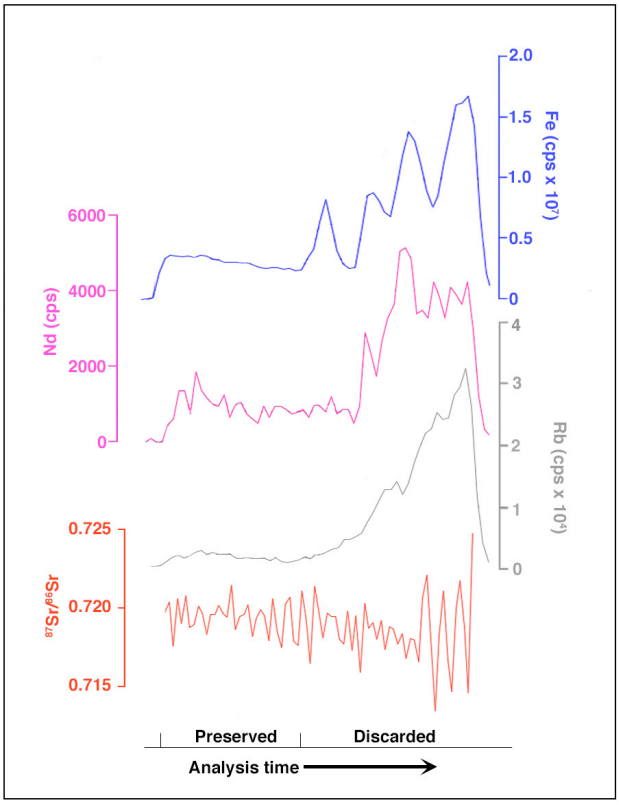

Figure 3. Demonstration of the utility of LASS for generating plagioclase-specific Sr isotopic data. In this analysis (spot 51 from crystal ALIA-115-18-2 in Supplementary Table 4), an inclusion of unknown affinity is encountered during the latter portion of the analysis. The inclusion is characterized by elevated Fe, REE (Nd is shown as an example), and Rb concentrations. The $^{87}Sr/^{86}Sr$ ratio is impacted by this inclusion, but simultaneous collection of major- and trace-element data via LASS allows us to reject the inclusion-influenced data. The figure shows counts per second (cps) for each element rather than concentration because the ^{43}Ca used as an internal standard is not the same in the plagioclase and the inclusion.

3. LASS $^{87}Sr/^{86}Sr$ measurements

The $^{87}Sr/^{86}Sr$ composition of plagioclase can be measured using LA-MC-ICP-MS with sufficient precision to resolve isotopic variability (Davidson et al., 2007); however, complicating factors include instrumental mass fractionation and isobaric interferences (Vroon et al., 2008). In practice, mass fractionation can be corrected by monitoring deviations from a canonical $^{86}Sr/^{88}Sr$ stable isotope ratio (0.1194), and correcting the measured $^{87}Sr/^{86}Sr$ ratio using the exponential mass fractionation law. However, isobaric

interferences on mass 86 from ^{86}Kr (present as a contaminant in the Ar carrier gas) can result in inaccurate measured $^{86}Sr/^{88}Sr$ and $^{87}Sr/^{86}Sr$ ratios. Therefore, in this study the Kr correction approach described by Konter and Storm (2014) was implemented to correct for Kr interferences. For a detailed description of this correction algorithm and of the MC-ICP-MS analytical procedures employed in this study, refer to Konter and Storm (2014) and the Supplementary Methods.

After correction for isobaric interferences (Kr and Rb; see Supplementary Methods) and mass fractionation, we used an in-house plagioclase primary reference material to correct the measured $^{87}Sr/^{86}Sr$ ratios of samples and secondary reference materials. This primary reference material, T21 (a homogenized plagioclase glass), was prepared by separating 450 mg of inclusion-free plagioclase chips from plagioclase-rich Samoan basalt sample T21 (see Workman et al., 2004). The plagioclase chips were powdered and fused twice in a 1500 °C furnace at Arizona State University, resulting in a homogeneous plagioclase glass (see Supplementary Table 1 for the major-element composition and Supplementary Table 2 for the trace-element composition of T21). The $^{87}Sr/^{86}Sr$ value of T21—determined via TIMS at the University of Leeds and corrected to an NBS987 $^{87}Sr/^{86}Sr$ value of 0.710240—is 0.704712 ± 0.000009 (2 SE) (see Table 2), which is similar to the whole-rock $^{87}Sr/^{86}Sr$ value of T21 (0.704751; Workman et al., 2004). The offset between the preferred TIMS and measured LASS $^{87}Sr/^{86}Sr$ values is calculated, and this offset (or "correction factor") is applied to all secondary reference materials and plagioclase samples using a linear interpolation. The magnitude of the correction factor (i.e., the difference between the measured and reference $^{87}Sr/^{86}Sr$ value of T21 for a given spot analysis) ranged from −1005 to +3 ppm during the course of this study. Following application of the correction factor, the

secondary reference materials measured during the course of this study yield precise and accurate $^{87}Sr/^{86}Sr$ ratios (see below).

Secondary reference materials for $^{87}Sr/^{86}Sr$ used in this study include a naturally homogeneous plagioclase crystal from the American Museum of Natural History, AMNH 107160 plagioclase ($^{87}Sr/^{86}Sr = 0.704386 \pm 0.000008$ [2 SE] via TIMS, Table 2; see Supplementary Table 1 for major-element analyses and Supplementary Table 2 for trace-element analyses), the USGS MACS-3 carbonate reference material ($^{87}Sr/^{86}Sr = 0.707546 \pm 0.000004$ [2 SE] via TIMS; Jochum et al., 2011), and a modern sclerosponge ($^{87}Sr/^{86}Sr$ of modern seawater = 0.709164 ± 0.000002 [2 SE] via TIMS; Mokadem et al., 2015). All $^{87}Sr/^{86}Sr$ values of the primary and secondary reference materials have been normalized to an NBS987 $^{87}Sr/^{86}Sr$ value of 0.710240.

LASS analyses were conducted during three analytical sessions on 3/2/2017, 5/8/2017, and 8/15/2017. A summary of all LASS and TIMS $^{87}Sr/^{86}Sr$ analyses of secondary reference materials—as well as analyses of a naturally homogeneous OIB-hosted plagioclase from Pitcairn sample Pit-16 (Garapić et al., 2015; see Supplementary Methods)—is available in Table 3, and $^{87}Sr/^{86}Sr$ (and major- and trace-element) data from each laser spot are available in Supplementary Table 3. Following correction to the preferred T21 value, the mean $^{87}Sr/^{86}Sr$ values of the three secondary $^{87}Sr/^{86}Sr$ reference materials agree with the reference values to better than 33 ppm. The reproducibility of measured $^{87}Sr/^{86}Sr$ was ± 260 ppm (2 SD, n=40) for the modern sclerosponge over three analytical sessions, ± 270 ppm (2 SD, n=40) for MACS-3 over three analytical sessions, and ± 353 ppm (2 SD, n=73) for AMNH 107160 plagioclase over two analytical sessions. The mean $^{87}Sr/^{86}Sr$ value measured by LASS for Pit-16 plagioclase agrees within 115 ppm of the value for the micromilled powder analyzed via TIMS (see Table 3, Supplementary Figure 3, and Supplementary Methods).

Reference materials and samples were analyzed using identic methods aside from the laser spot size and repetition rate, which we varied according to the Sr concentration of the analyte. The T21 primary reference material (1306 ppm Sr; Supplementary Table 2) and the AMNH 107160 secondary reference material (968 ppm) have lower Sr concentrations than the ALIA-115-18 (2054 ± 461 ppm, 2 SD**;** Supplementary Table 4) and the ALIA-115-21 (2218 ± 656 ppm, 2 SD) plagioclase crystals. During the analytical sessions, we analyzed the T21 and AMNH 107160 plagioclase reference materials every fourth sample analysis, and the MACS-3 and sclerosponge reference materials every twentieth sample analysis.

4. LASS major- and trace-element measurements

We measured the major- and trace-element compositions of plagioclase by LASS. See the Supplementary Methods section for a detailed description of LASS trace-element measurement procedures and the accuracy and reproducibility of LASS major- and trace-element measurements of reference materials. Major- and trace-element concentrations obtained by LASS used ^{43}Ca as an internal standard. For T21 plagioclase, AMNH 107160 plagioclase, Pit-16 plagioclase, and all Samoan plagioclase crystals analyzed by LASS in this study, Ca concentration was determined from EPMA measurements and then converted to ^{43}Ca.

C. Data and observations

We targeted six individual plagioclase crystals from Samoan lava samples ALIA-115-18 and ALIA-115-21. A summary of all ^{87}Sr/^{86}Sr, trace-element, and major-element geochemical data obtained on these plagioclase crystals is in Supplementary Table 4. All ^{87}Sr/^{86}Sr measurements are summarized in Figure 5, and plagioclase ^{87}Sr/^{86}Sr results are

compared to whole-rock and clinopyroxene $^{87}Sr/^{86}Sr$ values previously obtained from samples ALIA-115-18 and ALIA-115-21 (Jackson et al., 2009, 2007). We identify plagioclase domains with $^{87}Sr/^{86}Sr$ compositions that extend to values both lower and higher than those identified in host whole rocks and in clinopyroxene from the same lavas (Figure 5). Notably, we find significant intra-crystal isotopic heterogeneity in most of the plagioclase crystals that in some cases exceeds the analytical reproducibility of LASS $^{87}Sr/^{86}Sr$ measurements of reference materials by over an order of magnitude.

1. Description of individual crystals and geochemical characteristics

ALIA-115-18 plagioclase: The three plagioclase crystals from Samoan lava ALIA-115-18 targeted here are approximately 2 mm x 0.5 mm in size, and are characterized by the presence of fine oscillatory zoning that is visible in the quantitative EPMA maps of each grain (Supplementary Figure 1). The morphology and geochemical data collected for individual plagioclase crystals from ALIA-115-18 are described below.

ALIA-115-18-1: This plagioclase has a rounded, resorbed core with olivine and clinopyroxene inclusions along the outer edge of the core (see Supplementary Figure 1 for EPMA maps of this crystal). The average anorthite content (An = molar Ca/[Ca + Na] · 100) of this crystal at locations corresponding to each of the laser spots is 59 ± 2 (2 SD, using EPMA data compiled in Supplementary Table 4). We measured the $^{87}Sr/^{86}Sr$ and trace-element composition of this plagioclase in 75 spot locations over three analytical sessions. This plagioclase exhibits coherent $^{87}Sr/^{86}Sr$ zoning: a low-$^{87}Sr/^{86}Sr$ core is surrounded by a high-$^{87}Sr/^{86}Sr$ mantle, and a thin (c. 100 μm) low-$^{87}Sr/^{86}Sr$ rim (Figure 4). Small (c. 20–30 μm) olivine inclusions occur in the plagioclase within the high-$^{87}Sr/^{86}Sr$ zone near the

boundary with the low $^{87}Sr/^{86}Sr$ core (Figure 4). The $^{87}Sr/^{86}Sr$ values measured in this plagioclase range from 0.71853 ± 0.00032 (2SE) to 0.72239 ± 0.00027 (2SE); the measured $^{87}Sr/^{86}Sr$ range is approximately 5300 ppm. As with the other plagioclase crystals in this study, Sr shows an inverse relationship with $^{87}Sr/^{86}Sr$ though An content remains relatively constant (see section 3.2 and Figure 6). This anticorrelation is also demonstrated in Figure 4, wherein the low-$^{87}Sr/^{86}Sr$ core has elevated Sr concentrations, and the high-$^{87}Sr/^{86}Sr$ region has lower Sr concentrations.

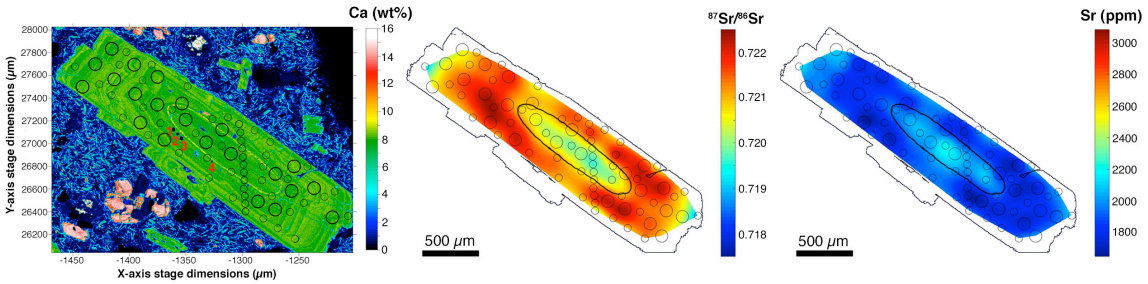

Figure 4. Quantitative Ca concentration map (left), $^{87}Sr/^{86}Sr$ model surface (middle), and Sr concentration model surface (right) for plagioclase ALIA-115-18-1. The Ca EPMA map was produced using CalcImage, and the $^{87}Sr/^{86}Sr$ and Sr concentration surfaces were generated using Matlab® (see Supplementary Methods). In each image, the location of the laser spots is indicated by circles with sizes corresponding to the laser spot size (see Supplementary Figure 1 for the Ca map with laser spot numbers added). The four olivine inclusions measured by EPMA spot analyses are indicated with red numbers in the EPMA image (see Table 1 for the olivine compositions). The olivines occur just outside of the rounded and resorbed core in a zone referred to in the text as the "olivine-bearing zone" which corresponds to high $^{87}Sr/^{86}Sr$ (and thus the plagioclase in this olivine-bearing zone samples the extreme EM2 "common component" shown in Figure 6). The boundary between the core and the rest of the crystal (the "core-mantle boundary) is visible as an irregular yellow line in the left panel. Lines indicating the crystal's edge and the "core-mantle boundary" are drawn on the model surfaces in the middle and right panels. Analogous figures for the other five Samoan plagioclase crystals from this study are shown in Supplementary Figure 2, and EPMA elemental maps for other major elements (Si, Al, Na, etc.) are shown in Supplementary Figure 1.

The mean $^{87}Sr/^{86}Sr$ value of four analyses made near the zone where olivine inclusions occur (called the "olivine-bearing zone" hereafter) is 0.72194 ± 0.00057 (2 SE), indistinguishable from (i.e., within uncertainty of) the highest value (0.72239 ± 0.00027 [2 SE]; Supplementary Table 4) reported in this study. The $^{87}Sr/^{86}Sr$ analyses made in the high-$^{87}Sr/^{86}Sr$ olivine-bearing zone are annotated in Figure 6. We targeted four olivine inclusions with EPMA spot analyses (see Table 1) in order to calculate the equilibrium melt Mg# associated with the olivines. The analyzed olivines have a mean forsterite content (= molar $Mg/[Mg+ Fe^{2+}] \cdot 100$) of 74.5 ± 0.8 (2 SD, N=4 different olivine inclusions). Assuming an olivine-melt K_D of 0.3 (where $K_D = [Fe^{2+}/Mg]_{olivine}/[Fe^{2+}/Mg]_{melt}$; Roeder and Emslie, 1970), this olivine was in equilibrium with a melt with Mg# = 46.8 ± 0.4 (2 SD) (where Mg# is molar $Mg/[Mg+Fe^{2+}] \cdot 100$). An uncertainty of 10% in the K_D value (i.e., calculate the equilibrium melt Mg# using a K_D of 0.27 and 0.33) yields a range in calculated equilibrium Mg# of 44 to 49, which is depicted by the error bars shown in Figure 7). Olivine-liquid Fe-Mg partitioning is sensitive to pressure, with K_D and pressure exhibiting a positive relationship; the K_D uncertainty used here spans a range from 1 atm to approximately 1.3 GPa (Ulmer, 1989).

ALIA-115-18-2: Plagioclase ALIA-115-18-2 contains multiple isolated regions of concentric anorthite zoning surrounded by a rim. The mean An content of this crystal is 59 ± 3 (2 SD) at the location of the laser spots (see data in Supplementary Table 4), the same value as the ALIA-115-18-1 plagioclase. We measured the $^{87}Sr/^{86}Sr$ composition of this plagioclase in 52 spot locations over two analytical sessions on 5/7/2017 and 8/15/2017. EPMA elemental maps of this sample were generated after the first (but before the second) laser ablation analytical session; therefore, we used the mean Ca concentration from the locations of the laser spots from the second analytical session as an internal standard to

calculate trace-element concentrations from the first laser-ablation analytical session. The Ca concentration of this crystal is quite homogeneous—8.12 ± 0.45 wt% (2 SD, n=40), so this approximation introduces minimal additional uncertainty to the trace-element concentrations. The range (5700 ppm) in $^{87}Sr/^{86}Sr$ values measured in this plagioclase (0.71792 ± 0.00028 [2 SE] to 0.72205 ± 0.00024 [2SE]) is greater than that measured in any of the other plagioclase crystals in this study. This crystal has a core characterized by low $^{87}Sr/^{86}Sr$, a mantle with moderate $^{87}Sr/^{86}Sr$, and a rim with high $^{87}Sr/^{86}Sr$ (Supplementary Figure 2).

ALIA-115-18-3: Plagioclase crystal ALIA-115-18-3 has an irregular core surrounded by a region characterized by oscillatory major-element zoning (Supplementary Figure 1). The An content of this crystal is 58 ± 3 (2 SD, n=31) determined at the location of each of the laser spots (Supplementary Table 4) is similar to the preceding two ALIA-115-18 plagioclase crystals. We measured the $^{87}Sr/^{86}Sr$ and trace-element composition of this crystal in 30 locations over two analytical sessions. The measured $^{87}Sr/^{86}Sr$ values in this sample range from 0.71789 ± 0.00024 (2 SE) to 0.72111 ± 0.00031 (2 SE); the measured range of $^{87}Sr/^{86}Sr$ is approximately 4400 ppm. This crystal has the lowest measured $^{87}Sr/^{86}Sr$ in this study (0.71789), but no measured $^{87}Sr/^{86}Sr$ values as high as those observed in the other two ALIA-115-18 plagioclase crystals (Figure 5). In contrast to the two previously described crystals from ALIA-115-18, this crystal has a core with high $^{87}Sr/^{86}Sr$ that is surrounded by a mantle with lower $^{87}Sr/^{86}Sr$.

ALIA-115-21 plagioclase: We measured the $^{87}Sr/^{86}Sr$, major-element, and trace-element composition of three plagioclase crystals from Samoan lava ALIA-115-21, and found that

the crystals exhibit more variability in An content (both higher and lower An values) than the ALIA-115-18 crystals (see lower panel of Figure 6). Additionally, although the ALIA-115-21 crystals extend to $^{87}Sr/^{86}Sr$ values as high as those observed in plagioclase from ALIA-115-18, the ALIA-115-21 plagioclase have less variable $^{87}Sr/^{86}Sr$ and do not extend to the low $^{87}Sr/^{86}Sr$ values observed in the ALIA-115-18 crystals. Compared to ALIA-115-18 plagioclase, a greater proportion of ALIA-115-21 LASS analyses reveal the presence of non-plagioclase inclusions or cracks; nonetheless, LASS enables us to reject or trim such analyses (e.g., Figure 3). We describe each crystal in turn below.

ALIA-115-21-1: This plagioclase is 1.5 mm x 0.3 mm in size. This crystal has a large, Ca-rich core (An as high as 54) surrounded by a Na-rich rim (An as low as 45). The mean An content from the laser spots is 50 ± 7 (2 SD; see Supplementary Table 4), which is quite variable and lower than the other plagioclase crystals examined in this study (Figure 6). The $^{87}Sr/^{86}Sr$ ratios in this plagioclase extend from 0.72078 ± 0.00028 (2 SE) to 0.72232 ± 0.00021 (2 SE) (range >2100 ppm).

ALIA-115-21-2: Plagioclase ALIA-115-21-2 is a glomerocryst of three individual plagioclase crystals; additional, smaller crystals are present, but were not analyzed. Two of the three large crystals have notably Ca-rich cores (see Ca EPMA map in Supplementary Figure 1). This glomerocryst has the highest anorthite content of any plagioclase targeted here (64), with an average An content of 58 ± 6 (2 SD, n=23) from the locations of the laser spots (Figure 6; Supplementary Table 4). Of all of the Samoan plagioclase evaluated here, ALIA-115-21-2 has the least isotopic variability (Figure 5). The mean $^{87}Sr/^{86}Sr$ of this plagioclase is 0.72216 ± 0.00026 (2 SD, n=23 spots), and $^{87}Sr/^{86}Sr$ ranges from 0.72180 ±

0.00023 (2 SE) to 0.72235 ± 0.00028 (2 SE). At 762 ppm, the range of measured $^{87}Sr/^{86}Sr$ values is approximately twice the 2 SD reproducibility achieved for the AMNH 107160 plagioclase reference material.

ALIA-115-21-3: Plagioclase ALIA-115-21-3 is a glomerocryst consisting of a larger crystal intergrown with at least two smaller crystals. The glomerocryst is approximately 2 mm x 0.5 mm in size. Each sub-crystal exhibits major-element zoning (see Supplementary Figure 1), but the anorthite content calculated at the location of each laser spot in this plagioclase shows limited variability relative to the other ALIA-115-21 plagioclase (mean An=54 ± 2 [2 SD], n=20; Supplementary Table 4). Of the three crystals from ALIA-115-21, this crystal exhibits the greatest variability in measured $^{87}Sr/^{86}Sr$ (Figure 5), with $^{87}Sr/^{86}Sr$ values ranging from 0.71982 ± 0.00031 to 0.72192 ± 0.00015 (range = 2910 ppm). There is a high-$^{87}Sr/^{86}Sr$ zone near the center of the largest crystal, but the zone is poorly defined owing to relatively few measurements with lower $^{87}Sr/^{86}Sr$ near the periphery of the crystal (Supplementary Figure 2).

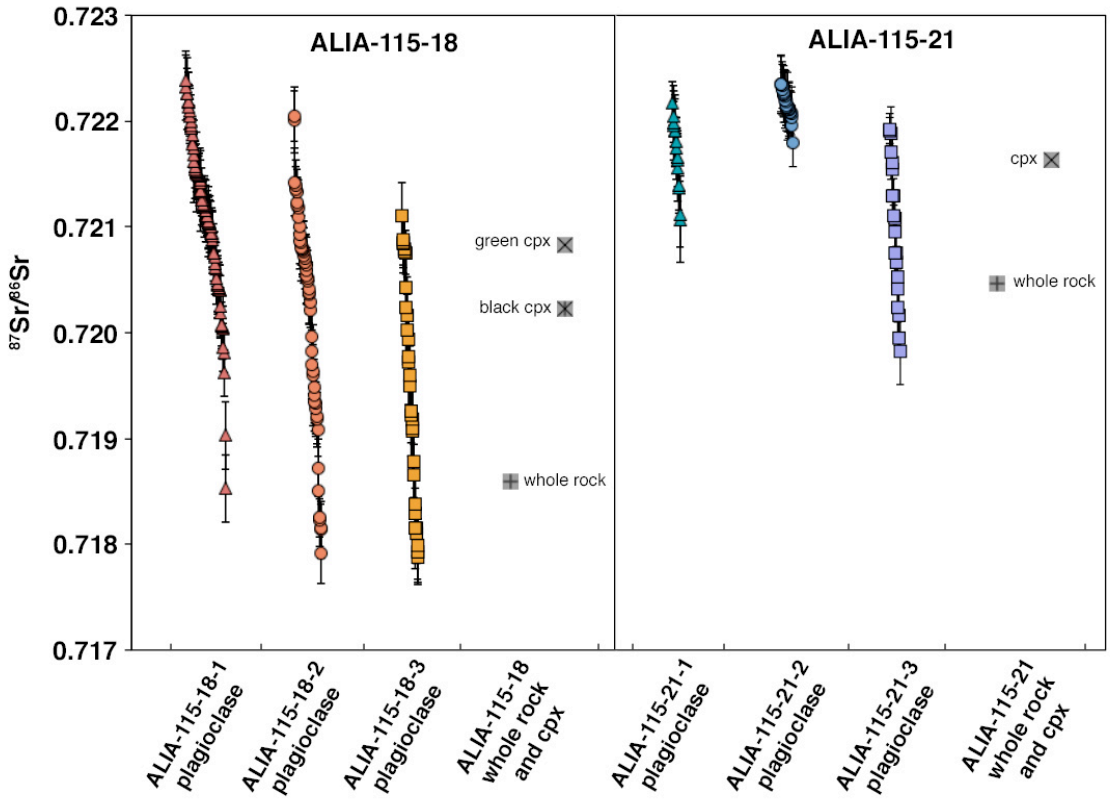

Figure 5. LASS $^{87}Sr/^{86}Sr$ data from the six Samoan plagioclase targeted in this study (see Supplementary Table 4 for the $^{87}Sr/^{86}Sr$ values and uncertainties used to make the figure). Error bars are internal 2SE. Whole-rock (Jackson et al. [2007]) and cpx (Jackson et al. [2009]) values from each lava (shown as squares) are plotted adjacent to the respective plagioclase data.

2. Geochemical trends recorded in plagioclase

Here we identify geochemical features of the LASS and EPMA data obtained for the Samoan plagioclase we targeted in this study.

The LASS data define a clear negative relationship between Sr and $^{87}Sr/^{86}Sr$ in the Samoan plagioclase crystals targeted. The data from each crystal define a unique slope, but all share the trend of higher $^{87}Sr/^{86}Sr$ at lower Sr concentration (Figure 6). Each crystal's array trends toward a common region characterized by high $^{87}Sr/^{86}Sr$. This extreme high-

$^{87}Sr/^{86}Sr$ EM2 component is more radiogenic than any Samoan whole rocks or mineral phases analyzed to date.

The presence of olivine inclusions (c. 20–30 μm) in a domain of a plagioclase that exhibits extremely radiogenic $^{87}Sr/^{86}Sr$ allows us to calculate the Mg# of the melt in equilibrium with the olivine and, by extension, the EM2 endmember sampled by the plagioclase assuming that the plagioclase and included olivine crystallized from the same homogeneous melt. The composition of the EM2 endmember observed in the plagioclase is relatively evolved: the Mg# of a melt in equilibrium with the olivines included in plagioclase ALIA-115-18-1 is 46.8 ± 0.4 (2 SD). When this composition is plotted with all Samoan lavas from the ALIA-115 dredge, the common component EM2 composition anchors the high-$^{87}Sr/^{86}Sr$ portion of the array (Figure 7).

However, other trace elements analyzed here (e.g., Rb, Ba, Ti, Y, REEs) do not exhibit the same clear relationships with $^{87}Sr/^{86}Sr$; La is shown as an example in Figure 6. Similarly, the anorthite composition of the plagioclase at each laser spot does not show a relationship with $^{87}Sr/^{86}Sr$ (Figure 6).

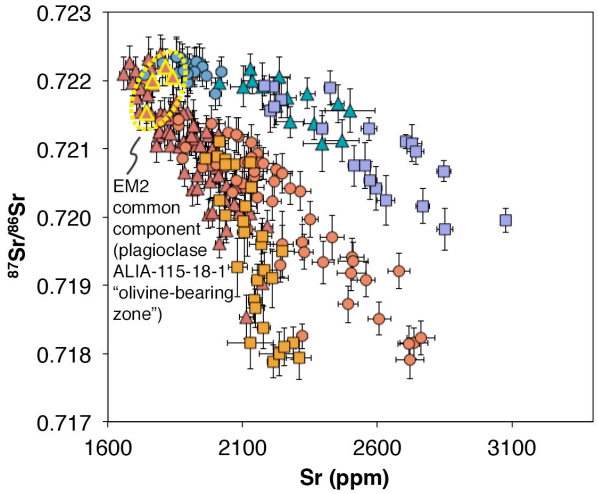
0.723
0.722
0.721
0.720
0.719
0.718
0.717
87Sr/86Sr
EM2
common
component
(plagioclase
ALIA-115-18-1
"olivine-bearing
zone")
1600
2100
2600
3100
Sr (ppm)

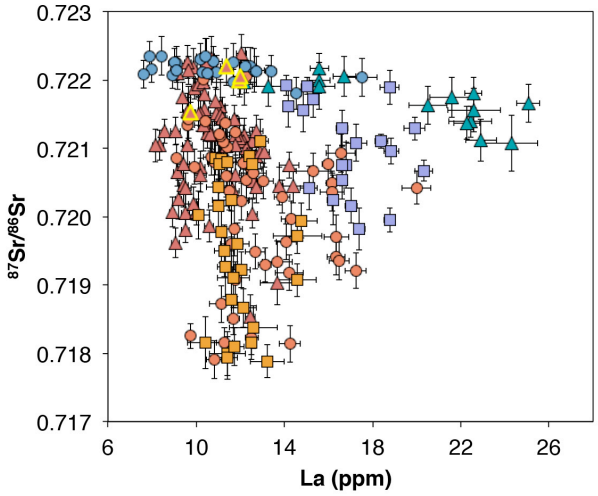
0.723
0.722
0.721
0.720
0.719
0.718
0.717
87Sr/86Sr
6
10
14
18
22
26
La (ppm)

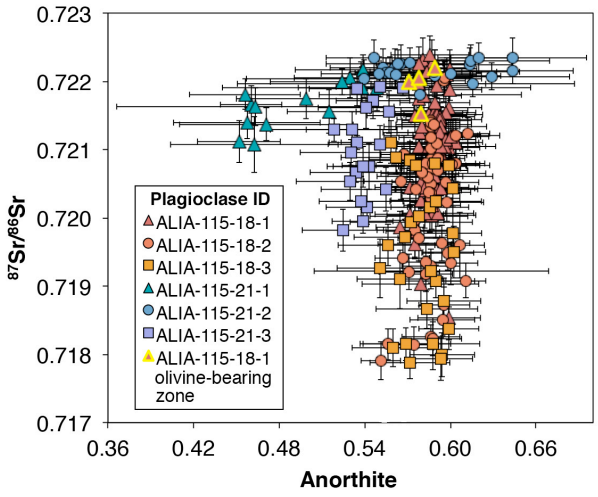
0.723
0.722
0.721
0.720
0.719
0.718
0.717
87Sr/86Sr
Plagioclase ID
ALIA-115-18-1
ALIA-115-18-2
ALIA-115-18-3
ALIA-115-21-1
ALIA-115-21-2
ALIA-115-21-3
ALIA-115-18-1
olivine-bearing
zone
0.36
0.42
0.48
0.54
0.60
0.66
Anorthite

Figure 6. Samoan plagioclase data from this study plotted in $^{87}Sr/^{86}Sr$–Sr space (top panel), $^{87}Sr/^{86}Sr$–La space (middle panel), and $^{87}Sr/^{86}Sr$–anorthite space (lower panel). Analyses from the olivine-bearing zone in plagioclase ALIA-115-18-1 are shown with yellow outlines. We selected the "olivine-bearing zone" plagioclase analyses by choosing laser spots from the zone nearest the olivine inclusions. We avoided laser spots that overlap with or contact the resorption surface itself because these analyses capture both the high-$^{87}Sr/^{86}Sr$ zone of the crystal and the low-$^{87}Sr/^{86}Sr$ core (and thus only four laser spot analyses are used to define the $^{87}Sr/^{86}Sr$ of the olivine zone). The "common component" that the plagioclase crystals trend toward in $^{87}Sr/^{86}Sr$–Sr space is circled in the top panel with a dashed yellow line. $^{87}Sr/^{86}Sr$, Sr, and La error bars are internal 2 SE. Anorthite (An = molar Ca/[Ca+Na]) compositions are averages calculated from quantitative EPMA maps of each plagioclase crystal (see Supplementary Figure 1 for EPMA maps). The anorthite error bars are calculated by propagating one standard deviation of the Na and Ca measurements at the location of each laser spot. All data shown in the figure are reported in Supplementary Table 4.

D. Discussion

Two of the six Samoan plagioclase crystals examined here contain the most extreme EM2 signatures ($^{87}Sr/^{86}Sr$ up to 0.7224) ever observed in OIB, and these new, ultrahigh $^{87}Sr/^{86}Sr$ signatures surpass the highest values previously reported in Samoan whole rocks (up to 0.720469) and in magmatic clinopyroxene (up to 0.721630). Furthermore, five of the six plagioclase crystals have extreme $^{87}Sr/^{86}Sr$ heterogeneity (>1500 ppm) that complements the intra-lava $^{87}Sr/^{86}Sr$ heterogeneity measured in plagioclase from mid-ocean ridge basalts (Lange et al., 2013), between olivine-hosted melt inclusions and their host OIB whole rocks (e.g., Jackson and Hart, 2006; Harlou et al., 2009; Sobolev et al., 2011; Reinhard et al., 2016), and between magmatic clinopyroxene and their host OIB whole rocks (e.g., Hanyu and Nakamura, 2000; Jackson et al., 2009; Hanyu et al., 2011).

The Samoan plagioclase investigated here sample an EM2 component with a radiogenic $^{87}Sr/^{86}Sr$ (=0.7224) signature more extreme than that observed in any other mantle-derived oceanic lavas. Below we rule out assimilation and post-eruptive radiogenic ingrowth as processes generating the extreme radiogenic isotopic compositions, and then explore the

implications of these new extreme EM compositions observed in Samoan plagioclase. The new extreme EM2 composition recorded in the plagioclase is calculated to be more evolved than any extreme EM2 lava examined to date from the Samoan ALIA-115 dredge, and its radiogenic $^{87}Sr/^{86}Sr$ composition requires that a higher fraction of recycled sediment was added to its source.

1. Origin of $^{87}Sr/^{86}Sr$ heterogeneity in Samoan plagioclase

The observation of intra-crystal $^{87}Sr/^{86}Sr$ disequilibrium in OIB is one of the salient findings of this study. Therefore, it is important to consider the mechanisms that may have been responsible for generating the $^{87}Sr/^{86}Sr$ heterogeneity in the plagioclase crystals we studied.

Varying degrees of radiogenic ingrowth of ^{87}Sr due to post-eruptive ^{87}Rb decay in the plagioclase cannot generate the extreme $^{87}Sr/^{86}Sr$ heterogeneity in the plagioclase crystals we measured. The lowest (0.00052) and highest (0.0068) measured Rb/Sr ratios from any two ALIA-115 plagioclase spots would lead to $^{87}Sr/^{86}Sr$ differences in the plagioclase of only 2 ppm over the 5.3 Myr (Koppers et al., 2008) since the plagioclase formed. Radiogenic ingrowth of ^{87}Sr is thus not the mechanism responsible for generating $^{87}Sr/^{86}Sr$ variability in these plagioclase crystals.

Assimilation of altered oceanic crust is not likely to have generated the extreme high $^{87}Sr/^{86}Sr$ observed in the Samoan plagioclase (which have $^{87}Sr/^{86}Sr \geq 0.71788$; see Supplementary Table 4), as the $^{87}Sr/^{86}Sr$ signature of altered oceanic crust only rarely achieves $^{87}Sr/^{86}Sr$ values that approach or exceed (e.g., Hauff et al., 2003), the value of seawater (0.709164; renormalized from Mokadem et al., 2015). Similarly, assimilation of seafloor sediments is not likely to have generated the extreme $^{87}Sr/^{86}Sr$ signatures observed here. Pb is highly enriched in marine sediments (Plank and Langmuir, 1998) compared to

oceanic lavas (Willbold and Stracke, 2006), so sediment assimilation would have a disproportionate influence on the Pb isotopic composition of a lava. This is notable because the Samoan EM2 lavas from ALIA dredge 115 form an array in $\Delta^{207}Pb/^{204}Pb–\Delta^{208}Pb/^{204}Pb$ space that diverges away from the field of modern sediments (Figure 4 of Jackson et al., 2007), and the extreme EM2 lavas with the highest $^{87}Sr/^{86}Sr$ plot farthest from the field defined by sediments in this Pb isotopic space. This observation suggests that the assimilation of modern seafloor sediments cannot have generated the enriched $^{87}Sr/^{86}Sr$ signatures in the whole rocks and, by extension, their plagioclase cargo.

One possible mechanism for generating intra-crystal $^{87}Sr/^{86}Sr$ heterogeneity may be mixing of two (or more) isotopically distinct melts. Each plagioclase crystal examined here defines a different negatively sloping array in $^{87}Sr/^{86}Sr$–Sr space (Figure 6), and a key observation is that all the arrays converge toward a common high-$^{87}Sr/^{86}Sr$ EM2 component. If mixing was responsible for generating these converging arrays, one or more low-$^{87}Sr/^{86}Sr$ endmembers (with higher Sr concentrations) may have mixed with a common high-$^{87}Sr/^{86}Sr$ component to generate the negatively sloping arrays in Figure 6. Textural features in the plagioclase support this hypothesis: plagioclase ALIA-115-18-1 (which exhibits the second most extreme degree of intra-crystal $^{87}Sr/^{86}Sr$ variability) has a rounded and resorbed core surrounded by a narrow olivine-bearing zone (Figure 4), features consistent with magma mixing. An important issue to address is the petrological characteristics of the magmas that mixed to generate the arrays observed in Figure 6.

2. A new extreme EM2 signature in an evolved melt: evidence for mixing an evolved EM2 magma with less-evolved magmas with lower $^{87}Sr/^{86}Sr$

Fortuitously, olivine (mean Fo = 74.5 ± 0.8, 2 SD) included in plagioclase ALIA-115-18-1—within a zone characterized by high $^{87}Sr/^{86}Sr$—allow us to calculate the Mg# of the EM2 common component magma to be Mg# = 46.8 ± 0.4 (2 SD). We thus infer that the extreme EM2 lava from which the olivine and plagioclase crystallized was relatively evolved. For comparison, a primary melt in equilibrium with Fo_{90} mantle olivine has a Mg# of 73.

This is an important observation because the calculated composition of the EM2 common component lies on an extension of the trend defined by the ALIA-115 whole rocks in $^{87}Sr/^{86}Sr$-Mg# space (Figure 7): the new extreme EM2 common component has an even lower calculated Mg# and higher measured $^{87}Sr/^{86}Sr$ ($^{87}Sr/^{86}Sr$=0.72194 ± 0.00057 [2 SD, N=4 spots]) than recorded in ALIA-115 whole-rock lavas. Because all of the lavas that form the compositional array in Figure 7 are from the same submarine dredge site off the coast of Savai'i island and presumably are petrogenetically linked, we explore a mechanism to explain the relationship between $^{87}Sr/^{86}Sr$ and Mg# in Figure 7.

We propose a conceptual model that mirrors the proposed mechanism for formation of the $^{87}Sr/^{86}Sr$–Sr trend illustrated in Figure 6: binary mixing of an evolved high-$^{87}Sr/^{86}Sr$ EM2 melt and a less evolved, low-$^{87}Sr/^{86}Sr$ melt (see the right panel of Figure 7 for a graphical description). In the model, two geochemically distinct primary mantle melts must be generated, one with low $^{87}Sr/^{86}Sr$ and one with high $^{87}Sr/^{86}Sr$. However, none of the lavas from the ALIA-115 dredge are primary melts (i.e., all lavas from ALIA dredge 115 have Mg# ≤ 65), so they are likely to have experienced variable degrees of magmatic evolution (i.e., fractional crystallization) in the crust prior to eruption. This is a reasonable assumption because even if the extreme EM2 melt with high $^{87}Sr/^{86}Sr$ initially had a Mg# of less than ~73 owing to the contribution of sediment to its source, it is likely that this melt would react

with ambient mantle peridotite and achieve a higher Mg# in equilibrium with mantle peridotite during transit through the mantle lithosphere (the nature of the extreme EM2 melt and its evolution during transit through the lithosphere is a topic, however, that warrants further investigation). In this dredge, the high-$^{87}Sr/^{86}Sr$ lavas are more evolved than the low-$^{87}Sr/^{86}Sr$ lavas (Figure 7). Thus, in the model, a more evolved high-$^{87}Sr/^{86}Sr$ melt and a less evolved low-$^{87}Sr/^{86}Sr$ melt mix, producing an array of intermediate compositions. The ALIA dredge 115 lavas and the extreme EM2 common component sampled by the Samoan plagioclase in this study define a trend in $^{87}Sr/^{86}Sr$-Mg# space that is consistent with this possible model (Figure 7). We emphasize that this is one possible model that can explain the observed geochemical trend; for example, it is possible that subducting sediment melts directly, and this melt is mixed with a peridotite-derived melt before being expressed as EM2 lavas in Samoa. Due to the divergence of Samoan EM2 lavas from seafloor sediments in Pb-isotope space, however, we consider this scenario to be less likely than one in which ancient sediment (with a Pb-isotopic composition unlike modern marine sediment) survives subduction and is mixed with mantle peridotite to generate a "hybrid" mantle source.

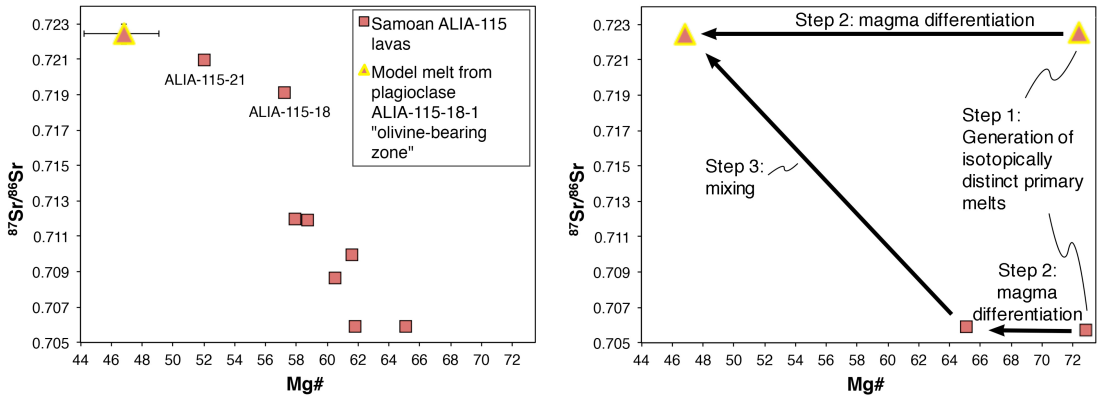

Figure 7. Left panel: $^{87}Sr/^{86}Sr$ plotted against Mg# of ALIA dredge 115 whole-rock lavas. A red triangle representing the olivine-bearing zone from plagioclase ALIA-115-18-1 is also plotted: the $^{87}Sr/^{86}Sr$ value for the olivine-bearing zone from ALIA-115-18-1 is the mean measured $^{87}Sr/^{86}Sr$ value (0.72194 ± 0.00057, 2 SD) of four laser spots (numbers 29, 48, 57, and 73; see Supplementary Table 4) near the olivine-bearing zone

in this crystal that target the high-$^{87}Sr/^{86}Sr$ zone with the olivine inclusions. The Mg# (46.8 ± 0.4, 2 SD) shown for the olivine-bearing zone is a melt calculated to be in equilibrium with the average forsterite content (74.5 ± 0.8, 2 SD) measured by EPMA in four olivine inclusions (see Table 1 for olivine compositions and Figure 4 for an image of ALIA-115-18-1 with the olivine locations annotated). The Mg# calculation assumes an olivine-melt Fe-Mg K_D of 0.30 (Roeder and Emslie, 1970). The Mg# error bars represent 10% uncertainty in the partition coefficient. The Mg# shown for whole-rock lavas assumes that 90% of total Fe is Fe^{2+}. ALIA dredge 115 whole-rock data are from Jackson et al. (2007). Right panel: a conceptual model to explain the trend in the left panel. In this model, two isotopically distinct primary mantle melts with Mg# 73 are generated (step 1). Each of the melts evolves to lower Mg#'s; however, the melt with more radiogenic $^{87}Sr/^{86}Sr$ achieves a lower Mg# than the melt with lower $^{87}Sr/^{86}Sr$ (step 2; see Discussion). Finally, the two different melts mix to produce the trend seen in the left panel of this figure (step 3).

This conceptual model may also explain why $^{86}Sr/^{86}Sr$ is negatively correlated with Sr: the more-radiogenic mixing endmember is more evolved and is more likely to have experienced greater degrees of plagioclase fractionation. Owing to the compatibility of Sr in plagioclase, the removal of plagioclase from the most-evolved EM2 melts results in residual melt with lower Sr, whereas the less-evolved lavas with lower $^{87}Sr/^{86}Sr$ will have higher Sr concentrations. Although plagioclase fractionation exerts a powerful lever on magmatic Sr concentrations, the concentrations of other trace elements examined in this study will not be as strongly influenced by fractional crystallization of plagioclase (or olivine and clinopyroxene, the other phases identified in ALIA-115 lavas; Koppers et al., 2008). As a result, these other trace elements will not follow the same trends as Sr during magmatic evolution, thereby decoupling $^{86}Sr/^{86}Sr$ from other incompatible trace-element signatures. This mechanism may explain the lack of clear correlations between $^{87}Sr/^{86}Sr$ and other geochemical indicators. Alternatively, the clear relationship between $^{87}Sr/^{86}Sr$ and Sr concentrations—but not other trace-element concentrations (e.g., La in Figure 6)—may be explained by different cation diffusion rates in plagioclase. This is because diffusion may relax original geochemical profiles in the plagioclase to varying degrees during residence in

a magma chamber (see Supplementary Discussion), a process that may preserve relationships between $^{87}Sr/^{86}Sr$ and Sr (due to similar diffusion rates of Sr and Sr-isotopic signatures in plagioclase) while decoupling $^{87}Sr/^{86}Sr$ from other trace elements.

One remaining uncertainty concerns whether the EM2 endmember melt is universally evolved. Although the extreme EM2 mixing endmember sampled by the plagioclase is more evolved than other lavas from the Samoan dredge ALIA-115 locality (Figure 7), it is not clear whether all EM2 lavas with extreme high $^{87}Sr/^{86}Sr$ ratios should be evolved. In other words, do mafic, near-primary equivalents of the extreme Samoan EM2 composition identified in the plagioclase from ALIA-115-18 and ALIA-115-21 (with $^{87}Sr/^{86}Sr = 0.7224$) exist as submarine flows at the Samoan hotspot? Figure 7 (right panel) posits that a mafic parental melt for the extreme EM2 melt sampled by the ALIA-115-18 and ALIA-115-21 plagioclase existed, but this is uncertain. Mafic extreme EM2 lavas, if they exist, would enhance our understanding of this mantle endmember because they would enable investigation of primary melt phase equilibria and estimates of the temperature and pressure conditions of EM2 mantle melting.

3. Generation of an extreme EM2 composition via terrigenous sediment recycling

The high-$^{87}Sr/^{86}Sr$ signature identified in the most extreme EM2 Samoan ALIA-115 lavas has been interpreted to reflect the ancient recycling of upper continental crust-derived sediment subducted into the mantle (Jackson et al., 2007; White and Hofmann, 1982; Workman et al., 2008). Combining trace-element and isotopic constraints, Jackson et al. (2007) estimated that the terrigenous sediment protolith contributing to the Samoan EM2 mantle has an $^{87}Sr/^{86}Sr$ composition of 0.7421 (these authors assumed an upper continental crust Sr concentration of 320 ppm; Rudnick and Gao, 2003). They found that the addition of ~5% of a terrigenous sediment protolith (with elevated present-day $^{87}Sr/^{86}Sr$) to a depleted

peridotite source like that calculated for the most geochemically depleted lavas in Samoa ($^{87}Sr/^{86}Sr$ = 0.704650 and Sr concentration = 28.3 ppm; Jackson et al., 2007) could generate the geochemically enriched trace-element and $^{87}Sr/^{86}Sr$ signatures in the second most extreme EM2 lava from Samoa, ALIA-115-18 (Jackson et al., 2007). Using the same model parameters employed by Jackson et al. (2007), we calculate that 7.4 ± 0.2% sediment is required to generate the highest-measured plagioclase $^{87}Sr/^{86}Sr$ value (0.72239 ± 0.00027) in this study. In this simple model, the composition of the UCC-like sediment is unmodified during subduction. We emphasize that this model is employed because it can account for both the the trace-element and Sr-isotopic signatures of Samoan ALIA-115 lavas; however, we do not consider the calculated sediment composition or amount to be a unique solution. For example, if the subducting sediment was depleted in Sr relative to the upper continental crust (e.g., due to chemical weathering effects), more sediment would be required to explain the extreme EM2 signature observed in some Samoan lavas. Alternatively, the sediment may have a higher present-day $^{87}Sr/^{86}Sr$ ratio (owing to elevated Rb/Sr or early sediment addition to the mantle) than the value chosen by Jackson et al. (2007); in this scenario, less sediment is required to account for the extreme Samoan EM2 signature observed in the ALIA-115 plagioclase. Although this model is not a unique solution, it nonetheless demonstrates that a small degree of additional sediment is required relative to ALIA-115 whole-rock lavas (Jackson et al., 2007) to account for the extreme $^{87}Sr/^{86}Sr$ signatures measured in this study.

The bulk of marine sediment is derived from the continents: the primitive mantle–normalized trace-element pattern for global subducting sediment (GLOSS) is remarkably similar to estimates for the composition of upper continental crust, and an estimated 76 wt% of marine sediment has a terrigenous origin (Plank and Langmuir, 1998). Thus, subduction

of marine sediment contributes a strong continental signature to the mantle. Over geologic time, significant volumes of sediment have been introduced into the terrestrial mantle, with sediment subduction flux estimates ranging from 1.0 $km^3\ a^{-1}$ (von Huene and Scholl, 1991) to 1.65 $km^3\ a^{-1}$ (Clift et al., 2009). We estimate the net mass of sediment that has been added to Earth's mantle over geologic time as follows. We assume a sediment density of 2500 kg m^{-3}, use the lower sediment subduction flux estimate of von Huene and Scholl (1991), and assume that 90% of all subducting sediment is relaminated to the base of the continents or melted in arc volcanism (an estimate that provides a lower bound on the amount of sediment that is input to the mantle, and therefore, a lower bound on the importance of sediment for the chemical composition of the mantle; Hacker et al., 2011). Using a time of 3 Ga (based on a recent estimate for the timescale over which subduction has operated; Shirey and Richardson, 2011), we calculate that $7.5 \cdot 10^{20}$ kg of sediment has been added to the convecting mantle. This quantity of sediment is ~0.02% of the mantle by mass. Although this reservoir of subducted sediment is minor in terms of its mass fraction, it has an outsized geochemical importance: if we assume that the non-sediment portion of the mantle has the primitive composition proposed by McDonough and Sun (1995) and the sediment has a composition like GLOSS-II (Plank, 2013), then 1.7–2.8% of the most incompatible elements (Rb, Th, U, and K) are hosted in the subducted sediment reservoir, and 0.3–0.4% of the moderately incompatible elements (e.g., Sr and Nd) are hosted in this sediment-derived reservoir. This estimate gives a lower limit on the geochemical impact of sediment subduction on the incompatible-element budget of the mantle because the mantle has been partially depleted by the extraction of continental crust. If the bulk mantle has the same composition as the depleted mantle composition sampled by MORB (Salters and Stracke, 2004; Workman and Hart, 2005)—an estimate that provides an upper limit on the

geochemical influence of subducted sediment on the incompatible element budget of the mantle—then 7–33% of the most incompatible elements and 0.6–1% of the moderately incompatible elements reside in the subducted sediment domain. Thus, subducted sediment may play an important role in the geochemical budgets of highly incompatible elements, and therefore radiogenic heat production in Earth's interior.

Although 0.02% of the mass of the mantle may consist of recycled sediment, this sediment component is heterogeneously distributed: 7.4 ± 0.2% of the mantle source of the extreme EM2 domain sampled by the plagioclase in this study consists of recycled sediment. The survival of such sediment-rich domains in the mantle suggests that subducted sediment is not always efficiently mixed in the dynamically convecting mantle, and therefore, geochemical signatures imparted by subducted sediment are not efficiently attenuated. Instead, regions of the mantle can contain relatively high mass fractions of recycled sediment.

There is evidence that subducted sediment is concentrated in certain regions of Earth's mantle: Castillo (1988) found that hotspots exhibiting EM (enriched mantle) signatures are positioned above one of the two near-antipodal large low-shear-velocity provinces (LLSVPs) at the base of the mantle. If EM domains trace their origins to subducted sediment, the LLSVPs may represent regions that host unusually high concentrations of subducted sediment. If the LLSVPs compose 7.7% of the volume of the mantle by mass (Cottaar and Lekic, 2016), and if most of the subducted sediment is hosted in the LLSVPs, approximately 0.25% of the LLSVPs is composed of subducted sediment. This percentage is higher if, for example, the fraction of the mass fraction of the LLSVPs has been overestimated, or if the fraction of sediment that escapes relamination is higher. Nonetheless, the high mass fraction of sediment estimated in the Samoan extreme EM2

source (7.4 ± 0.2%) is anomalous, and reflects an unusual surviving relic of subducted sediment in the dynamically convecting mantle.

E. Conclusions

We report new $^{87}Sr/^{86}Sr$ measurements of plagioclase in extreme Samoan EM2 lavas. We employ laser-ablation split-stream mass spectrometry (LASS), which permits simultaneous analysis of trace-element concentrations and $^{87}Sr/^{86}Sr$ from the same crystal volume. We measure over 5000 ppm of intra-crystal $^{87}Sr/^{86}Sr$ heterogeneity in two of the six plagioclase samples examined here, which is significantly greater than the long-term analytical reproducibility achieved for a plagioclase reference material (± 350 ppm). Critically, we observe highly radiogenic $^{87}Sr/^{86}Sr$ ratios (up to 0.7224) in plagioclase from two different Samoan EM2 lavas, the highest $^{87}Sr/^{86}Sr$ ratios ever measured in oceanic lavas. This finding highlights the utility of microanalytical studies of single plagioclase crystals in revealing new, extreme mantle signatures in OIB lavas.

The simultaneous measurement of Sr isotopic and trace-element compositions of the plagioclase reveals a relationship between $^{87}Sr/^{86}Sr$ and Sr concentrations in the six plagioclase crystals analyzed here: data from each plagioclase crystal form a negatively sloping array in $^{87}Sr/^{86}Sr$–Sr space, and the arrays converge on a common enriched EM2 component. We interpret $^{87}Sr/^{86}Sr$ heterogeneity in the plagioclase—and the relationship between $^{87}Sr/^{86}Sr$ and Sr concentrations—to reflect mixing between an extremely enriched EM2 "common component" with at least one component with less radiogenic $^{87}Sr/^{86}Sr$. We calculate the Mg# of this extreme EM2 common component from the compositions of olivines (forsterite content 74.5 ± 0.8, 2 SD) hosted in a high-$^{87}Sr/^{86}Sr$ plagioclase zone that samples the EM2 common component: a melt in equilibrium with the olivines has a Mg# of

46.8 ± 0.4 (2 SD), indicating the extreme EM2 common component melt is relatively evolved. This new calculated EM2 endmember composition plots on an extension of the negatively sloping array formed by relevant Samoan whole-rock lavas in $^{87}Sr/^{86}Sr$–Mg# space, supporting the contention that extreme EM2 melts in Samoa are relatively evolved.

The discovery of a new extreme EM2 endmember composition provides a new maximum estimate of the amount of recycled terrigenous sediment sampled by an EM2 melt. The elevated $^{87}Sr/^{86}Sr$ recorded in Samoan plagioclase zones requires a high fraction of recycled sediment (7.4 ± 0.2%) in the Samoan mantle source. This fraction is significantly higher than our estimate for the fraction of Earth's mantle that is likely to be composed of recycled sediment (0.02%). The observation of a new extreme EM2 signature in plagioclase from the Samoan hotspot thus provides new insights on sediment recycling, an important process for generating heterogeneity in Earth's dynamic mantle.

References

1. Castillo, P., 1988. The Dupal anomaly as a trace of the upwelling lower mantle. Nature 336, 667–670. https://doi.org/10.1038/336667a0

2. Christensen, J.N., Halliday, A.N., Lee, D.-C., Hall, C.M., 1995. In situ Sr isotopic analysis by laser ablation. Earth Planet. Sci. Lett. 136, 79–85.

3. Clift, P.D., Vannucchi, P., Morgan, J.P., 2009. Crustal redistribution, crust-mantle recycling and Phanerozoic evolution of the continental crust. Earth-Science Rev. 97, 80–104. https://doi.org/10.1016/j.earscirev.2009.10.003

4. Cottaar, S., Lekic, V., 2016. Morphology of seismically slow lower-mantle structures. Geophys. J. Int. 207, 1122–1136. https://doi.org/10.1093/gji/ggw324

5. Davidson, J., Tepley, F., Palacz, Z., Meffan-Main, S., 2001. Magma recharge, contamination and residence times revealed by in situ laser ablation isotopic analysis of feldspar in volcanic rocks. Earth Planet. Sci. Lett. 184, 427–442. https://doi.org/10.1016/S0012-821X(00)00333-2

6. Davidson, J.P., Morgan, D.J., Charlier, B.L.A., Harlou, R., Hora, J.M., 2007. Microsampling and Isotopic Analysis of Igneous Rocks: Implications for the Study of Magmatic Systems. Ann. Rev. Earth Plan. Sci. 35, 273–311. https://doi.org/10.1146/annurev.earth.35.031306.140211

7. Davidson, J.P., Tepley, F.J., 1997. Recharge in volcanic systems: Evidence from isotope profiles of phenocrysts. Science (80-.). 275, 826–829. https://doi.org/10.1126/science.275.5301.826

8. Font, L., Davidson, J.P., Pearson, D.G., Nowell, G.M., Jerram, D.A., Ottley, C.J., 2008. Sr and Pb isotope micro-analysis of plagioclase crystals from skye lavas: An insight into open-system processes in a flood basalt province. J. Petrol. 49, 1449–1471. https://doi.org/10.1093/petrology/egn032

9. Garapić, G., Jackson, M.G., Hauri, E.H., Hart, S.R., Farley, K.A., Blusztajn, J.S., Woodhead, J.D., 2015. A radiogenic isotopic (He-Sr-Nd-Pb-Os) study of lavas from the Pitcairn hotspot: Implications for the origin of EM-1 (enriched mantle 1). Lithos 228–229, 1–11. https://doi.org/10.1016/j.lithos.2015.04.010

10. Gast, P.W., Tilton, G.R., Hedge, C., 1964. Isotopic Composition of Lead and Strontium from Ascension and Gough Islands. Science (80-.). 145, 1181–1185.

11. Hacker, B.R., Kelemen, P.B., Behn, M.D., 2011. Differentiation of the continental crust by relamination. Earth Planet. Sci. Lett. 307, 501–516. https://doi.org/10.1016/j.epsl.2011.05.024

12. Hanyu, T., Nakamura, E., 2000. Constraints on HIMU and EM by Sr and Nd isotopes re-examined. Earth, Planets Sp. 52, 61–70.

https://doi.org/10.1186/BF03351614

13. Hanyu, T., Tatsumi, Y., Senda, R., Miyazaki, T., Chang, Q., Hirahara, Y., Takahashi, T., Kawabata, H., Suzuki, K., Kimura, J.I., Nakai, S., 2011. Geochemical characteristics and origin of the HIMU reservoir: A possible mantle plume source in the lower mantle. Geochemistry, Geophys. Geosystems 12, 1–30. https://doi.org/10.1029/2010GC003252

14. Harlou, R., Pearson, D.G., Nowell, G.M., Ottley, C.J., Davidson, J.P., 2009. Combined Sr isotope and trace element analysis of melt inclusions at sub-ng levels using micro-milling, TIMS and ICPMS. Chem. Geol. 260, 254–268. https://doi.org/10.1016/j.chemgeo.2008.12.020

15. Hart, S.R., Schilling, J.-G., Powell, J.L., 1973. Basalts from Iceland and Along the Reykjanes Ridge: Sr Isotope Geochemistry. Nature 246, 104–107. https://doi.org/10.1038/10.1038/physci246104a0

16. Hauff, F., Hoernle, K., Schmidt, A., 2003. Sr-Nd-Pb composition of Mesozoic Pacific oceanic crust (Site 1149 and 801, ODP Leg 185): Implications for alteration of ocean crust and the input into the Izu-Bonin-Mariana subduction system. Geochemistry, Geophys. Geosystems 4. https://doi.org/10.1029/2002GC000421

17. Hofmann, A.W., 1997. Mantle geochemistry: the message from oceanic volcanism. Nature 385, 219–229.

18. Jackson, M.G., Hart, S.R., 2006. Strontium isotopes in melt inclusions from Samoan basalts: Implications for heterogeneity in the Samoan plume. Earth Planet. Sci. Lett. 245, 260–277. https://doi.org/10.1016/j.epsl.2006.02.040

19. Jackson, M.G., Hart, S.R., Koppers, A.A.P., Staudigel, H., Konter, J., Blusztajn, J., Kurz, M., Russell, J.A., 2007. The return of subducted continental crust in Samoan lavas. Nature 448, 684–687. https://doi.org/10.1038/nature06048

20. Jackson, M.G., Hart, S.R., Shimizu, N., Blusztajn, J.S., 2009. The $^{87}Sr/^{86}Sr$ and $^{143}Nd/^{144}Nd$ disequilibrium between Polynesian hot spot lavas and the clinopyroxenes they host: Evidence complementing isotopic disequilibrium in melt inclusions. Geochemistry, Geophys. Geosystems 10. https://doi.org/10.1029/2008GC002324

21. Jochum, K.P., Wilson, S.A., Abouchami, W., Amini, M., Chmeleff, J., Eisenhauer, A., Hegner, E., Iaccheri, L.M., Kieffer, B., Krause, J., Mcdonough, W.F., Mertz-Kraus, R., Raczek, I., Rudnick, R.L., Scholz, D., Steinhoefel, G., Stoll, B., Stracke, A., Tonarini, S., Weis, D., Weis, U., Woodhead, J.D., 2011. GSD-1G and MPI-DING Reference Glasses for In Situ and Bulk Isotopic Determination. Geostand. Geoanalytical Res. 35, 193–226. https://doi.org/10.1111/j.1751-908X.2010.00114.x

22. Konter, J.G., Storm, L.P., 2014. High precision $^{87}Sr/^{86}Sr$ measurements by MC-ICP-MS, simultaneously solving for Kr interferences and mass-based fractionation.

Chem. Geol. 385, 26–34. https://doi.org/10.1016/j.chemgeo.2014.07.009

23. Koppers, A.A.P., Russell, J.A., Jackson, M.G., Konter, J., Staudigel, H., Hart, S.R., 2008. Samoa reinstated as a primary hotspot trail. Geology 36, 435–438. https://doi.org/10.1130/G24630A.1

24. Koppers, A.A.P., Russell, J.A., Roberts, J., Jackson, M.G., Konter, J.G., Wright, D.J., Staudigel, H., Hart, S.R., 2011. Age systematics of two young en echelon Samoan volcanic trails. Geochemistry, Geophys. Geosystems 12. https://doi.org/10.1029/2010GC003438

25. Kylander-Clark, A.R.C., Hacker, B.R., Cottle, J.M., 2013. Laser-ablation split-stream ICP petrochronology. Chem. Geol. 345, 99–112. https://doi.org/10.1016/j.chemgeo.2013.02.019

26. Lange, A.E., Nielsen, R.L., Tepley, F.J., Kent, A.J.R., 2013. Diverse Sr isotope signatures preserved in mid-oceanic-ridge basalt plagioclase. Geology 41, 279–282. https://doi.org/10.1130/G33739.1

27. McDonough, W.F., Sun, S. -s., 1995. The chemical composition of the Earth. Chem. Geol. 120, 223–253. https://doi.org/10.1016/0009-2541(94)00140-4

28. Miyazaki, T., Hanyu, T., Kimura, J.I., Senda, R., Vaglarov, B.S., Chang, Q., Hirahara, Y., Takahashi, T., Kawabata, H., Sato, T., 2018. Clinopyroxene and bulk rock Sr–Nd–Hf–Pb isotope compositions of Raivavae ocean island basalts: Does clinopyroxene record early stage magma chamber processes? Chem. Geol. 482, 18–31. https://doi.org/10.1016/j.chemgeo.2017.12.015

29. Mokadem, F., Parkinson, I.J., Hathorne, E.C., Anand, P., Allen, J.T., Burton, K.W., 2015. High-precision radiogenic strontium isotope measurements of the modern and glacial ocean: Limits on glacial-interglacial variations in continental weathering. Earth Planet. Sci. Lett. 415, 111–120. https://doi.org/10.1016/j.epsl.2015.01.036

30. Paul, B., Woodhead, J.D., Hergt, J., Danyushevsky, L., Kunihiro, T., Nakamura, E., 2011. Melt inclusion Pb-isotope analysis by LA-MC-ICPMS: Assessment of analytical performance and application to OIB genesis. Chem. Geol. 289, 210–223. https://doi.org/10.1016/j.chemgeo.2011.08.005

31. Plank, T., 2013. The Chemical Composition of Subducting Sediments, in: Treatise on Geochemistry: Second Edition. Elsevier Ltd., pp. 607–629. https://doi.org/10.1016/B978-0-08-095975-7.00319-3

32. Plank, T., Langmuir, C.H., 1998. The chemical composition of subducting sediment and its consequences for the crust and mantle. Chem. Geol. 145, 325–394. https://doi.org/10.1016/S0009-2541(97)00150-2

33. Ramos, F.C., Wolff, J. A., Tollstrup, D.L., 2005. Sr isotope disequilibrium in Columbia River flood basalts: Evidence for rapid shallow-level open-system

processes. Geology 33, 457. https://doi.org/10.1130/G21512.1

34. Reinhard, A.A., Jackson, M.G., Harvey, J., Brown, C., Koornneef, J.M., 2016. Extreme differences in $^{87}Sr/^{86}Sr$ between Samoan lavas and the magmatic olivines they host: Evidence for highly heterogeneous $^{87}Sr/^{86}Sr$ in the magmatic plumbing system sourcing a single lava. Chem. Geol. 439, 120–131. https://doi.org/10.1016/j.chemgeo.2016.05.017

35. Roeder, P.L., Emslie, R.F., 1970. Olivine-liquid equilibrium. Contrib. to Mineral. Petrol. 29, 275–289. https://doi.org/10.1007/BF00371276

36. Rudnick, R.L., Gao, S., 2003. 3.01 - Composition of the Continental Crust. Treatise on Geochemistry 1, 1–64. https://doi.org/http://dx.doi.org/10.1016/B0-08-043751-6/03016-4

37. Saal, A.E., Hart, S.R., Shimizu, N., Hauri, E.H., Layne, G.D., 1998. Pb isotopic variability in melt inclusions from oceanic island basalts, Polynesia. Science (80-.). 282, 1481–1484.

38. Saal, A.E., Hart, S.R., Shimizu, N., Hauri, E.H., Layne, G.D., Eiler, J.M., 2005. Pb isotopic variability in melt inclusions from the EMI-EMII-HIMU mantle end-members and the role of the oceanic lithosphere. Earth Planet. Sci. Lett. 240, 605–620. https://doi.org/10.1016/j.epsl.2005.10.002

39. Salters, V.J.M., Stracke, A., 2004. Composition of the depleted mantle. Geochemistry, Geophys. Geosystems 5. https://doi.org/10.1029/2003GC000597

40. Shirey, S.B., Richardson, S.H., 2011. Start of the Wilson cycle at 3 Ga shown by diamonds from subcontinental mantle. Science (80-.). 333, 434–436. https://doi.org/10.1126/science.1206275

41. Sobolev, A. V., Hofmann, A.W., Jochum, K.P., Kuzmin, D. V., Stoll, B., 2011. A young source for the Hawaiian plume. Nature 476, 434–439. https://doi.org/10.1038/nature10321

42. Stracke, A., 2012. Earth's heterogeneous mantle: A product of convection-driven interaction between crust and mantle. Chem. Geol. 330–331, 274–299. https://doi.org/10.1016/j.chemgeo.2012.08.007

43. Ulmer, P., 1989. The dependence of the Fe2+-Mg cation-partitioning between olivine and basaltic liquid on pressure, temperature and composition - An experimental study to 30 kbars. Contrib. to Mineral. Petrol. 101, 261–273. https://doi.org/10.1007/BF00375311

44. von Huene, R., Scholl, D.W., 1991. Observations at convergent margins concerning sediment subduction, erosion, and the growth of continental crust. Rev. Geophys. 29, 279–316. https://doi.org/10.1029/91RG00969

45. Vroon, P.Z., van der Wagt, B., Koornneef, J.M., Davies, G.R., 2008. Problems in obtaining precise and accurate Sr isotope analysis from geological materials using laser ablation MC-ICPMS. Anal. Bioanal. Chem. 390, 465–476. https://doi.org/10.1007/s00216-007-1742-9

46. White, W., Hofmann, A., 1982. Sr and Nd isotope geochemistry of oceanic basalts and mantle evolution. Nature 296, 821–825. https://doi.org/10.1038/296821a0

47. White, W.M., 2015. Isotopes, DUPAL, LLSVPs, and Anekantavada. Chem. Geol. 419, 10–28. https://doi.org/10.1016/j.chemgeo.2015.09.026

48. Willbold, M., Stracke, A., 2006. Trace element composition of mantle end-members: Implications for recycling of oceanic and upper and lower continental crust. Geochemistry, Geophys. Geosystems 7, 1–30. https://doi.org/10.1029/2005GC001005

49. Workman, R.K., Eiler, J.M., Hart, S.R., Jackson, M.G., 2008. Oxygen isotopes in Samoan lavas: Confirmation of continent recycling. Geology 36, 551–554. https://doi.org/10.1130/G24558A.1

50. Workman, R.K., Hart, S.R., 2005. Major and trace element composition of the depleted MORB mantle (DMM). Earth Planet. Sci. Lett. 231, 53–72. https://doi.org/10.1016/j.epsl.2004.12.005

51. Workman, R.K., Hart, S.R., Jackson, M., Regelous, M., Farley, K.A., Blusztajn, J., Kurz, M., Staudigel, H., 2004. Recycled metasomatized lithosphere as the origin of the Enriched Mantle II (EM2) end-member: Evidence from the Samoan Volcanic Chain. Geochemistry, Geophys. Geosystems 5, 1–44. https://doi.org/10.1029/2003GC000623

52. Yurimoto, H., Kogiso, T., Abe, K., Barsczus, H.G., Utsunomiya, A., Maruyama, S., 2004. Lead isotopic compositions in olivine-hosted melt inclusions from HIMU basalts and possible link to sulfide components. Phys. Earth Planet. Inter. 146, 231–242. https://doi.org/10.1016/j.pepi.2003.08.013

53. Zindler, A., Hart, S.R., 1986. Chemical Geodynamics. Annu. Rev. Earth Planet. Sci. 14, 493–571. https://doi.org/10.1146/annurev.earth.14.1.493

Appendix

A. Supplementary Methods

1. Sample preparation

Sample preparation was performed at the University of California at Santa Barbara (UCSB). Hand samples were cut to expose fresh surfaces, plagioclase crystals were visually identified, and rock chips containing the plagioclase crystals were isolated using a small tile saw and a 150 μm diamond-wire saw. The isolated chips were mounted in one-inch epoxy rounds, ground flat with progressively finer silicon carbide abrasive paper, and polished with diamond polishing compounds until a 0.25 μm finish was achieved. After polishing, the mounts were coated with approximately 20 nm of carbon (following EPMA analysis and prior to LASS analysis, this carbon coating was removed).

2. EPMA mapping and spot analysis

Maps of each plagioclase crystal were generated by electron probe microanalysis (EPMA) using a Cameca SX-100 instrument at UCSB with a step size of 4 x 4 μm. EPMA quantitative elemental maps of Al, Ca, Na, Si, K, Fe, Mg, P, Sr, and Ti were prepared with CalcImage (Probe Software, Inc.) (see maps in Supplementary Figure 1). These EPMA maps were used to guide laser ablation spot placement, and the plagioclase compositions corresponding to each laser spot were calculated using Surfer® (Golden Software, LLC) and MATLAB® (The MathWorks, Inc.) (Supplementary Table 4).

The major-element compositions of two $^{87}Sr/^{86}Sr$ reference materials, T21 homogenized plagioclase and AMNH 107160, were also determined by EPMA. Both materials have homogeneous major-element (Supplementary Table 1) compositions. For both T21 and AMNH 107160, we used the Ca concentrations measured by EPMA (reported in

Supplementary Table 1) as the internal standard when calculating trace-element concentrations.

In one plagioclase crystal, ALIA-115-18-1, the compositions of olivine inclusions hosted within the plagioclase were determined using EPMA spot analyses. EPMA operating parameters during spot analysis consisted of a 40-degree takeoff angle, a 20 keV beam energy, a 40 nA beam current, and a 5 μm diameter beam. The EPMA analytical standards were synthetic MnO for Mn, Fe_2SiO_4 (synthetic fayalite) for Fe, Ni_2SiO_4 (synthetic) for Ni, Mg_2SiO_4 (synthetic magnesium olivine) for Mg and Si, Chesterman Diopside for Ca, MAD-10 Orthoclase for Al, and Chromite (UC # 523-9) for Cr. Results for each olivine are the average of 1 to 5 spots depending on the size of the olivine inclusion available for EPMA (Table 1); some olivines were cracked or round, limiting the surface area available for analysis. Oxygen was calculated by cation stoichiometry, and included in the matrix correction. The mass absorption coefficients used for matrix correction are from the FFAST dataset, and the Phi-rho-Z correction followed the method of Pouchou and Pichoir (1991).

3. LA-MC-ICP-MS

During $^{87}Sr/^{86}Sr$ analysis, the Faraday cups in the Nu *Plasma HR* mass spectrometer were configured to cover the Sr mass range and the intermediate half-masses to monitor the presence of doubly charged REE (Supplementary Table 5). Due to the extremely low abundances of the relevant interfering REE^{++} ($^{168}Yb^{++}$ and $^{168}Er^{++}$ on mass 84, $^{170}Yb^{++}$ and $^{170}Er^{++}$ on mass 85, $^{172}Yb^{++}$ on mass 86, $^{174}Yb^{++}$ on mass 87, and $^{176}Yb^{++}$ and $^{176}Lu^{++}$ on mass 88) in plagioclase relative to the high Sr abundances (see Supplementary Table 4), we did not perform a REE^{++} correction using the half-mass signal intensities. We measured all baselines 0.7 AMU below the mass of interest (Jackson and Hart, 2006), and used an ESA

deflection of the beam during baseline acquisition to obtain an "instrument zero". "On-peak" baselines were not used because we correct for Kr interference using the approach of Konter and Storm (2014) described below. We do not use the measured ^{82}Kr and ^{83}Kr intensities to make the correction for isobaric interferences from Kr, but we do report ^{83}Kr intensities in Supplementary Table 4 to demonstrate that Kr intensities were low during the analytical sessions.

The $^{87}Sr/^{86}Sr$ and trace-element compositions of samples and reference materials were measured in analytical blocks consisting of two baseline measurements, a series of primary and secondary reference materials measured at the beginning and end of each block, and alternating samples and reference materials throughout each block. With the laser off, baselines were measured for 60 seconds at the beginning and end of each block (where a block consists of analyses of multiple plagioclase and primary/secondary reference materials). A "working baseline" was interpolated throughout the block, and this baseline was applied to all analyses made during that block. After baseline measurement, the magnet was adjusted so the beam is in on-mass position to begin analysis of samples and reference materials. Samples and reference materials were then pre-ablated with a single pulse of the laser using the same spot size as used for analysis. Each pre-ablation was followed by a 45-second washout, followed by 30–45 seconds of sample analysis per laser spot. The sample stage was then moved to a subsequent spot where pre-ablation commenced after 5 seconds. The laser repetition rate and spot size varied depending on the concentration of Sr in the analyte: spot sizes ranged from 35 to 155 μm and repetition rates ranged from 10 to 60 Hz (laser spot sizes and repetition rates for all analyses are given in Supplementary Tables 3 and 4). After all reference materials and samples were analyzed, the magnet was again moved to its off-mass position, the beam was deflected using the ESA, and baselines were again

measured for 60 seconds. Analytical blocks ranged from 40 to 83 analyses over the course of the study.

The Kr correction approach of Konter and Storm (2014) was employed. Using baseline-corrected signal intensities, this method simultaneously solves for Kr and Sr mass fractionation and the amount of Kr "peak stripping" required to account for the offset between the measured and canonical $^{84}Sr/^{88}Sr$ (0.00675476) and $^{86}Sr/^{88}Sr$ (0.1194) ratios. We use a canonical—rather than empirical—$^{84}Kr/^{86}Kr$ ratio of 3.276 for this Kr correction. Rb was monitored on mass 85, and the ^{87}Rb isobaric interference on mass 87 was calculated using the exponential fractionation factor calculated for Sr and assuming an $^{87}Rb/^{85}Rb$ ratio of 0.38571. The calculated ^{87}Rb signal intensity was subtracted from the ^{87}Sr signal to generate an interference-corrected $^{87}Sr/^{86}Sr$ ratio. Finally, this interference-corrected $^{87}Sr/^{86}Sr$ ratio was corrected for mass fractionation using the exponential law.

All $^{87}Sr/^{86}Sr$ data were reduced using Iolite 2.5 (Paton et al., 2011). We used the Matlab function 'gridfit' (D'Errico, 2006) to depict the spatial distribution of $^{87}Sr/^{86}Sr$ and Sr concentration in the Samoan plagioclase. See Figure 4 and Supplementary Figure 2 for the interpolated surfaces generated for each plagioclase crystal.

4. Micromilling and TIMS analysis of plagioclase to test the accuracy of $^{87}Sr/^{86}Sr$ values obtained by LASS

We tested whether measured LASS $^{87}Sr/^{86}Sr$ ratios from a natural, OIB-hosted plagioclase agree with the $^{87}Sr/^{86}Sr$ value measured on the same crystal by TIMS. We micromilled a large plagioclase crystal from Pitcairn lava Pit-16, a moderately enriched ($^{87}Sr/^{86}Sr$ of the whole rock = 0.704687) trachybasalt (Garapić et al., 2015). The Pit-16 plagioclase was determined to be isotopically homogeneous within the LASS analytical

precision reported in this study: based on 19 separate spot analyses of the crystal, the Pit-16 plagioclase crystal yielded a measured $^{87}Sr/^{86}Sr$ ratio of 0.70442 ± 0.00018 (2 SD; Table 3). This crystal was micromilled at UCSB following the method of Charlier et al. (2006) with an ESI® *Micromill*. After Sr purification following standard column-chemistry separation techniques and TIMS analysis at the University of Leeds, the measured $^{87}Sr/^{86}Sr$ value of the powder was 0.704505 ± 0.000012 (2 SE; Table 2). The total Sr blank of 149 pg—the sum of the total chemistry procedural blank of 52 pg Sr, and the micromilling blank of 97 pg Sr—is insignificant relative to the estimated total Sr in the micromilled powder (approximately 49 ng). The TIMS $^{87}Sr/^{86}Sr$ value obtained for the Pit-16 micromilled powder overlaps with the mean LASS value within uncertainty, demonstrating that we are able to accurately reproduce the measured $^{87}Sr/^{86}Sr$ TIMS value of a natural plagioclase crystal using LASS.

We also micromilled a portion of the T21 homogenized plagioclase glass primary reference materials and a portion of the AMNH 107160 plagioclase secondary reference materials to ensure that measured $^{87}Sr/^{86}Sr$ values obtained for micromilled powders agree with values obtained from plagioclase chips. We obtained an $^{87}Sr/^{86}Sr$ value of 0.704699 ± 0.000018 via TIMS for the T21 micromilled powder (Table 2), which is indistinguishable from the TIMS reference value of 0.704712 ± 0.000009 (2 SE) obtained by dissolution of a 4.2 mg chip of this reference material (Table 2). For the AMNH 107160 plagioclase micromilled powder, we obtained an $^{87}Sr/^{86}Sr$ value of 0.704408 ± 0.000020 (2 SE) (Table 2), which agrees within uncertainty with the TIMS reference value of 0.704386 ± 0.000008 obtained by dissolution of a 2.0 mg chip of this plagioclase (Table 2). Finally, the LASS $^{87}Sr/^{86}Sr$ values obtained for the ANMH 107160 plagioclase reference material (0.704373 ± 0.000249, 2 SD, n=83) agree with the $^{87}Sr/^{86}Sr$ values obtained on this plagioclase by TIMS for both a plagioclase chip and a micromilled powder. Thus, within analytical precision,

micromilling does not influence the measured $^{87}Sr/^{86}Sr$ composition of plagioclase analyzed in this study.

5. LASS major- and trace-element accuracy and reproducibility

We measured the major- and trace-element composition from each laser spot via LASS. ^{43}Ca was used as the internal standard, and BHVO-2G was used as a primary reference material (reference trace-element concentrations for BHVO-2G are from Jochum et al., 2005). MPI-DING basaltic glasses ML3-B and KL-2 (reference concentrations from Jochum et al., 2006) were treated as secondary reference materials to assess data quality. We measured these geologic reference materials twice each during each block of analyses: once at the beginning, and once at the end. The LA-Q-ICP-MS concentrations for ML3-B and KL-2 are compared with the preferred concentrations in Supplementary Table 2. Additionally, the homogeneous T21 plagioclase was used as a phase-specific secondary reference material: trace-element concentrations were obtained for four separate fragments of the T21 plagioclase by wet chemistry and Q-ICP-MS at Aarhus University, Denmark, and the results are compared with the trace-element concentrations obtained by LASS in Supplementary Table 2. We also present initial trace-element concentrations for the AMNH 107160 plagioclase in Supplementary Table 2, although no reference values are available at this time. The measured concentrations from each LASS analysis of these reference materials are available in Supplementary Table 3. All trace-element data were reduced in Iolite 2.5 using the "internal standard" trace-element data reduction scheme (Paton et al., 2011).

Long-term average concentrations for all elements analyzed by LASS in the basaltic glass reference materials KL2-G and ML3B-G (n=26 analyses for both reference materials)

agree with published reference values within 8% (Supplementary Table 2). Reproducibility for most elements analyzed by LASS was better than 9% (2 RSD) except for Lu, with 2 RSD = 10.1% for KL2-G and 2 RSD = 11.3% for ML3B-G. Long-term average concentrations for most elements measured by LASS in the T21 homogenized plagioclase reference material (n=95 analyses) agree with the preliminary reference values obtained via solution ICP-MS and EPMA within 10%. K and Rb are two notable elements for which LASS results show only modest agreement with EPMA and solution ICP-MS preliminary reference values (the difference is 16% and 34%, respectively) in the T21 plagioclase. The reproducibility of Rb (2 RSD = 31.1%) is not as good as the other elements examined here, but we report measured Rb concentrations to demonstrate that the Rb/Sr ratios in the plagioclase are low and thus isobaric ^{87}Rb interferences can be effectively corrected. We emphasize that the Rb concentration measured by LASS was not used to correct for the interference of ^{87}Rb when measuring ^{87}Sr/^{86}Sr ratios. We also report heavy REEs that exhibit low concentrations and relatively poor analytical reproducibility for the T21 plagioclase (see Supplementary Table 2) to demonstrate that REE^{++} isobaric interferences in the Sr mass range are negligible.

Because the ALIA-115-18 and ALIA-115-21 plagioclase crystals we analyzed are not homogeneous with respect to their major-element compositions, the mean Ca concentration of the plagioclase at the location of each laser spot—determined by extraction from quantitative EPMA Ca concentration maps—was used as the internal elemental standard. However, EPMA concentrations for ALIA-115-18-2 are unavailable at the location of the laser spots from the analytical session on 5/8/2017 because this plagioclase was analyzed by LASS before an EPMA map of the crystal was prepared. For this crystal we used the mean measured Ca concentration from the locations of the laser spots from a latter analytical

session (8.12 ± 0.45 wt%, n=40) as the internal standard for trace-element analyses from 5/8/2017.

Concentrations of a suite of elements (Si, Na, K, Fe, Mg, Al, and Sr) were determined for the Samoan plagioclase by two methods: EPMA (which uses compositions extracted from EPMA maps at the location of each laser spot) and LASS (which quantifies the elemental concentrations in the volume of crystal that was analyzed via laser ablation). The two methods measure concentrations from two different portions of the crystal: the EPMA method gives compositions at the *crystal surface* targeted by the laser, whereas the LASS method provides an average composition from the *volume* ablated by the laser. Therefore, the observation that the EPMA and LASS measurements exhibit relatively good agreement in the Samoan plagioclase (see Supplementary Table 4) suggests that downhole geochemical zonation in the Samoan plagioclase crystals does not significantly affect the geochemical data presented here.

B. Supplementary Discussion: cation diffusion in plagioclase.

Here, we discuss the role that diffusion may play in decoupling $^{87}Sr/^{86}Sr$ from other geochemical signatures in the Samoan plagioclase we studied. There is a strong relationship between valence state and cation diffusion rates in plagioclase, whereby univalent cations diffuse most rapidly, divalent cations diffuse at intermediate rates, and trivalent cations diffuse most slowly (Cherniak, 2003). Therefore, in plagioclase, Sr diffuses more rapidly than the trivalent REE but more rapidly than the alkali elements. Sr also diffuses significantly more rapidly than the timescales on which CaAl-NaSi interdiffusion in plagioclase occurs (Costa et al., 2003; Grove et al., 1984). There is also a relationship between ionic radius and diffusion whereby larger cations diffuse more slowly (e.g., Ba

diffuses more slowly than Sr; Cherniak, 2002). Thus, if Sr zones in the plagioclase we studied have "blurred" by diffusion over magma chamber timescales, $^{87}Sr/^{86}Sr$ would not be expected to correlate with trace elements that diffuse at significantly different rates than Sr.

Although the rates of chemical and tracer (i.e., isotopic) diffusion of Sr in silicate melts differ by over an order of magnitude (Baker, 1989), similar rates of Sr chemical and tracer diffusion have been determined for plagioclase (Cherniak and Watson, 1994). Therefore, the Sr concentration and $^{87}Sr/^{86}Sr$ profiles in the plagioclase should track each other, but may be more or less diffusively relaxed than the profiles of trace elements or anorthite content. Below, we explore whether diffusion could plausibly decouple $^{87}Sr/^{86}Sr$ from other geochemical signatures in the Samoan plagioclase in this study using previously published cation diffusion parameters and geologically reasonable estimates for temperature.

Following Cherniak (2003), we estimate the time required to lose cation zoning in plagioclase. In this approach, zones are modeled as sheets of thickness l with a different concentration of a given element than the surrounding medium. The diffusion coefficient is given by D, and time is t. Cherniak (2003) defined a dimensionless parameter ($=Dt/l^2$) that allows one to calculate the time at which concentrations in a region of a zone are changed by a certain amount. When the dimensionless parameter Dt/l^2 is equal to $3.3 \cdot 10^{-2}$, the concentration at the center of the zone is modified by 10%. At this point, Cherniak's model considers a zone to be lost (2003). Although this criterion for loss of zonation is somewhat arbitrary, it provides a way to estimate the timescales required to lose plagioclase zoning for specific elements, and hence the timescales over which their geochemical signatures become decoupled by diffusion.

Given a temperature of 1000 °C, we estimate the timescales over which 100 μm zones are lost in plagioclase for various cations to evaluate whether diffusion can decouple

$^{87}Sr/^{86}Sr$ from other trace-element concentrations. We use diffusion coefficients from plagioclase experiments that most closely approximate the compositions of the Samoan plagioclase in this study (i.e., labradorite), but we note that the paucity of experimental data prevent us from choosing diffusion parameters from studies with identical plagioclase compositions and experimental procedures. We are also unable to calculate timescales of zoning loss for elements with unexplored diffusion behavior in plagioclase (although inferences from valence state and radius can be drawn).

Univalent cations diffuse most rapidly in plagioclase: 100 μm K zoning is estimated to be lost in < 1 year in $An_{62.6}$ plagioclase at 1000 °C, using the diffusion parameters of Giletti and Shanahan (1997). Although Giletti and Shanahan (1997) did not evaluate Rb diffusion in labradorite, they determine that the diffusivities for Rb and K are similar in albite, with Rb diffusing more slowly. Divalent cations diffuse more slowly than univalent cations: at 1000 °C, 100 μm Sr zones would be lost in ~10 years in An_{67} plagioclase (Cherniak and Watson, 1994), and Ba zones would be lost in approximately 800 years in An_{67} plagioclase at 1000 °C (Cherniak, 2002). Finally, 100 μm trivalent REE zones would be lost in ~10,000 years at 1000 °C in An_{67} plagioclase (Cherniak, 2003). CaAl-NaSi interdiffusion proceeds even more slowly: CaAl-NaSi zones in $An_{80–81}$ plagioclase would be lost in ~15 Ma at 1000 °C (Grove et al., 1984).

Over shorter timescales (at a given temperature), zoning patterns in plagioclase are "blurred" rather than lost. The aforementioned dimensionless parameter Dt/l^2 describes this "blurring" when it equals $1.8 \cdot 10^{-3}$ (Cherniak, 2003). At this point, the composition of the zone 10% from its surface (i.e., at a depth of $l/10$) has changed by 10%. Using the same zone size (100 μm) and temperature (1000 °C) as above, we calculate that univalent cation zones would be blurred in 17 days, Sr zones would be blurred in 0.6 years, Ba zones would

be blurred in 50 years, REE zones would be blurred in 700 years, and CaAl-NaSi zones would be blurred in ~800,000 years.

Although we do not attempt to reconstruct plagioclase residence times here (see Zellmer et al., 1999), these example calculations demonstrate that at geologically reasonable timescales and temperatures, diffusion may blur zones in plagioclase at sufficiently different rates to decouple $^{87}Sr/^{86}Sr$ from other geochemical signatures (e.g., Rb, K, REE, anorthite). This observation may explain why $^{87}Sr/^{86}Sr$ does not correlate with these trace-element or major-element indices. In contrast, $^{87}Sr/^{86}Sr$ and Sr concentration signatures diffusively relax at similar rates, a phenomenon that is perhaps responsible for preserving the trends between $^{87}Sr/^{86}Sr$ and Sr in the Samoan plagioclase we studied.

References

1. Baker, D.R., 1989. Tracer vs. trace element diffusion: diffusional decoupling of Sr concentration fron Sr isotope composition. Geochim. Cosmochim. Acta 53, 3015–3023.

2. Charlier, B.L.A., Ginibre, C., Morgan, D., Nowell, G.M., Pearson, D.G., Davidson, J.P., Ottley, C.J., 2006. Methods for the microsampling and high-precision analysis of strontium and rubidium isotopes at single crystal scale for petrological and geochronological applications. Chem. Geol. 232, 114–133. https://doi.org/10.1016/j.chemgeo.2006.02.015

3. Cherniak, D.J., 2003. REE diffusion in feldspar. Chem. Geol. 193, 25–41. https://doi.org/10.1016/S0009-2541(02)00246-2

4. Cherniak, D.J., 2002. Ba diffusion in feldspar. Geochim. Cosmochim. Acta 66, 1641–1650. https://doi.org/10.1016/S0016-7037(01)00866-3

5. Cherniak, D.J., Watson, E.B., 1994. A study of strontium diffusion in plagioclase using Rutherford backscattering spectroscopy. Geochim. Cosmochim. Acta 58, 5179–5190. https://doi.org/10.1016/0016-7037(94)90303-4

6. Costa, F., Chakraborty, S., Dohmen, R., 2003. Diffusion coupling between major and trace elements and a model for the calculation of magma chamber residence times using plagioclase. Geochim. Cosmochim. Acta 67, 2189–2200. https://doi.org/10.1016/S0016-7037(00)01345-5

7. D'Errico, J.R., 2006. Understanding Gridfit.

8. Garapić, G., Jackson, M.G., Hauri, E.H., Hart, S.R., Farley, K.A., Blusztajn, J.S., Woodhead, J.D., 2015. A radiogenic isotopic (He-Sr-Nd-Pb-Os) study of lavas from the Pitcairn hotspot: Implications for the origin of EM-1 (enriched mantle 1). Lithos 228–229, 1–11. https://doi.org/10.1016/j.lithos.2015.04.010

9. Giletti, B.J., Shanahan, T.M., 1997. Alkali diffusion in plagioclase feldspar. Chem. Geol. 139, 3–20. https://doi.org/10.1016/S0009-2541(97)00026-0

10. Grove, T.L., Baker, M.B., Kinzler, R.J., 1984. Coupled CaAl-NaSi diffusion in plagioclase feldspar: Experiments and applications to cooling rate speedometry. Geochim. Cosmochim. Acta 48, 2113–2121. https://doi.org/10.1016/0016-7037(84)90391-0

11. Jackson, M.G., Hart, S.R., 2006. Strontium isotopes in melt inclusions from Samoan basalts: Implications for heterogeneity in the Samoan plume. Earth Planet. Sci. Lett. 245, 260–277. https://doi.org/10.1016/j.epsl.2006.02.040

12. Jochum, K.P., Stoll, B., Herwig, K., Willbold, M., Hofmiann, A.W., Amini, M., Aarburg, S., Abouchami, W., Hellebrand, E., Mocek, B., Raczek, I., Stracke, A., Alard, O., Bouman, C., Becker, S., Dücking, M., Brätz, H., Klemd, R., De Bruin, D., Canil, D., Cornell, D., De Hoog, C.J., Dalpé, C., Danyushevshy, L., Eisenhauer, A., Gao, Y., Snow, J.E., Groschopf, N., Günther, D., Latkoczy, C., Guillong, M., Hauri, E.H., Höfer, H.E., Lahaye, Y., Horz, K., Jacob, D.E., Kasemann, S.A., Kent, A.J.R., Ludwig, T., Zack, T., Mason, P.R.D., Meixner, A., Rosner, M., Misawa, K., Nash, B.P., Pfänder, J., Premo, W.R., Sun, W.D., Tiepolo, M., Vannucci, R., Vennemann, T., Wayne, D., Woodhead, J.D., 2006. MPI-DING reference glasses for in situ microanalysis: New reference values for element concentrations and isotope ratios. Geochemistry, Geophys. Geosystems 7. https://doi.org/10.1029/2005GC001060

13. Jochum, K.P., Willbold, M., Raczek, I., Stoll, B., Herwig, K., 2005. Chemical Characterisation of the USGS Reference Glasses GSA-1G, GSC-1G, GSD-1G, GSE-1G, BCR-2G, BHVO-2G and BIR-1G Using EPMA, ID-TIMS, ID-ICP-MS and LA-ICP-MS. Geostand. Geoanalytical Res. 29, 285–302. https://doi.org/10.1111/j.1751-908X.2005.tb00901.x

14. Konter, J.G., Storm, L.P., 2014. High precision 87Sr/86Sr measurements by MC-ICP-MS, simultaneously solving for Kr interferences and mass-based fractionation. Chem. Geol. 385, 26–34. https://doi.org/10.1016/j.chemgeo.2014.07.009

15. Paton, C., Hellstrom, J., Paul, B., Woodhead, J., Hergt, J., 2011. Iolite: Freeware for the visualisation and processing of mass spectrometric data. J. Anal. At. Spectrom. 26, 2508–2518. https://doi.org/10.1039/c1ja10172b

16. Pouchou, J.-L., Pichoir, F., 1991. Quantitative analysis of homogeneous or stratified microvolumes applying the model "PAP," in: Electron Probe Quantitation. Springer,

pp. 31–75.

17. Zellmer, G.F., Blake, S., Vance, D., Hawkesworth, C., Turner, S., 1999. Plagioclase residence times at two island arc volcanoes (Kameni Islands, Santorini, and Soufriere, St. Vincent) determined by Sr diffusion systematics. Contrib. to Mineral. Petrol. 136, 345–357. https://doi.org/10.1007/s004100050543

C. Supplementary figures

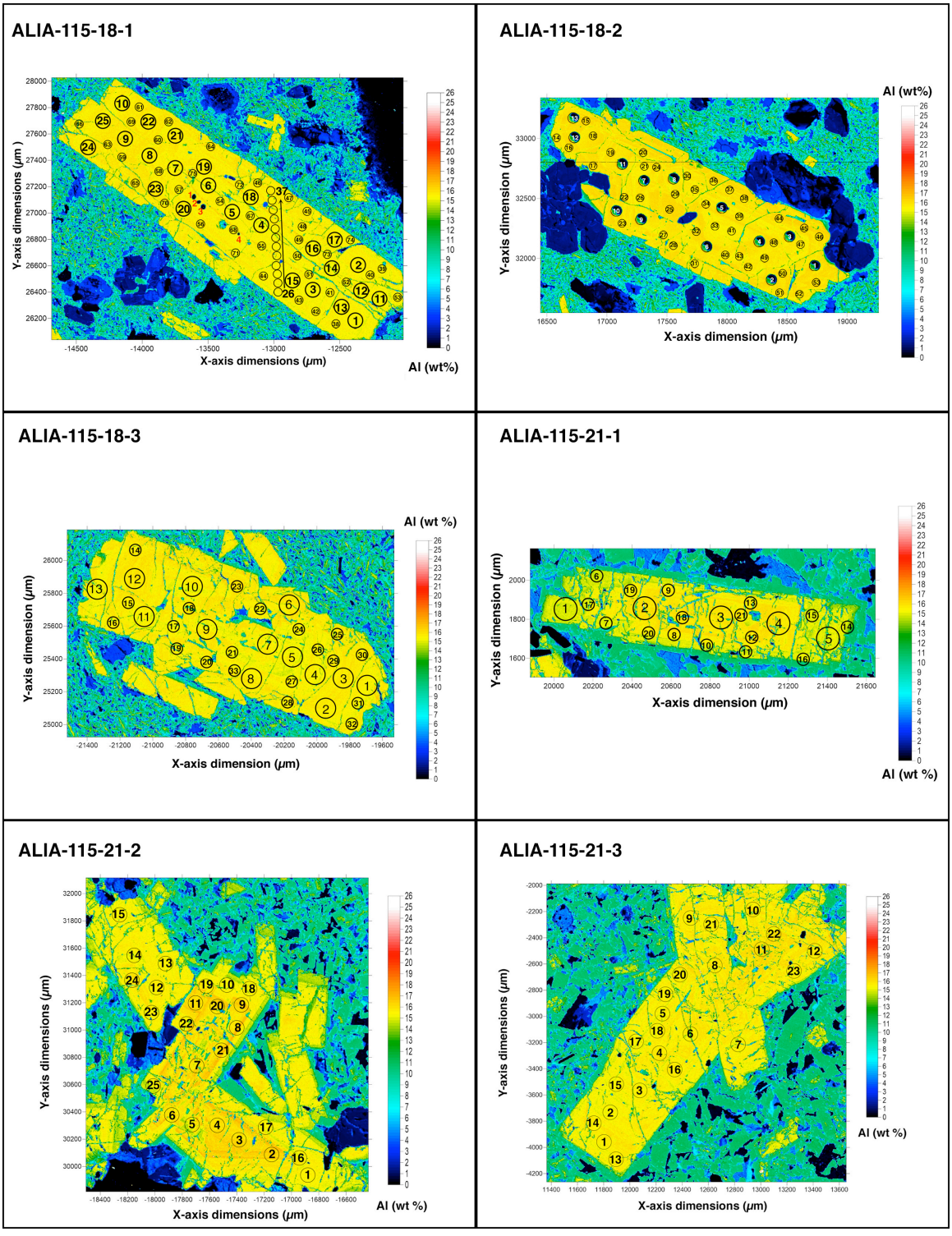

ALIA-115-18-1

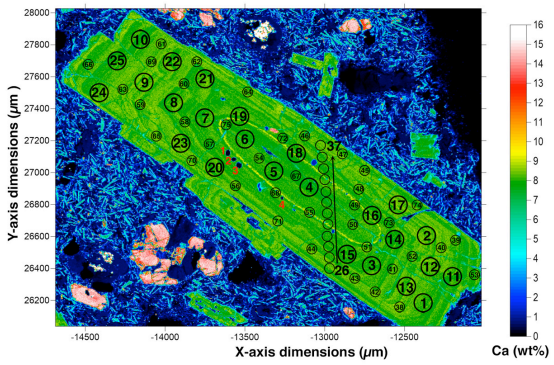

ALIA-115-18-2

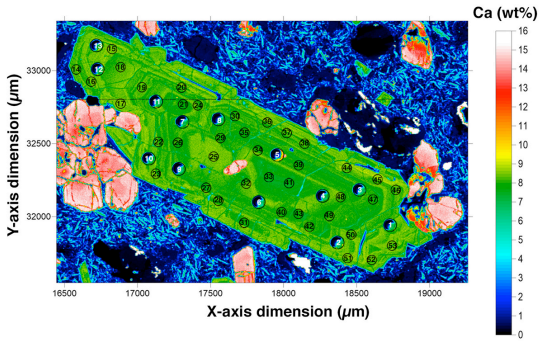

ALIA-115-18-3

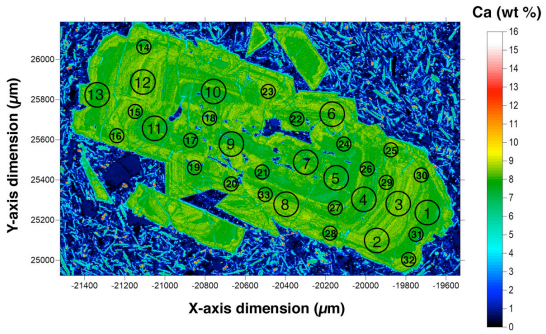

ALIA-115-21-1

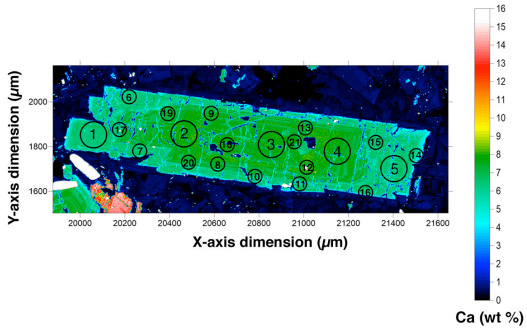

ALIA-115-21-2

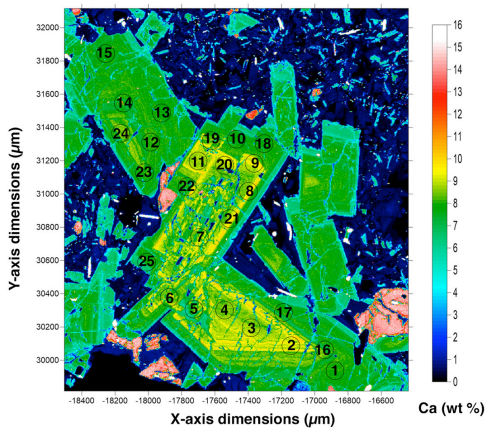

ALIA-115-21-3

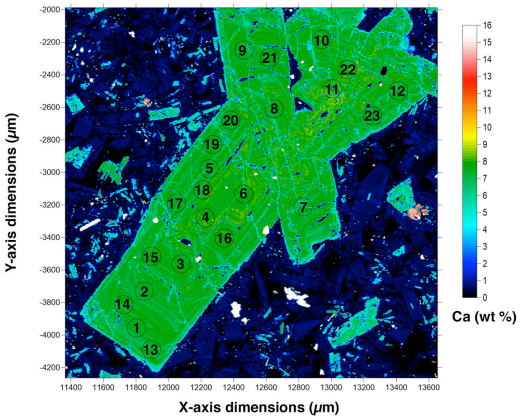

ALIA-115-18-1

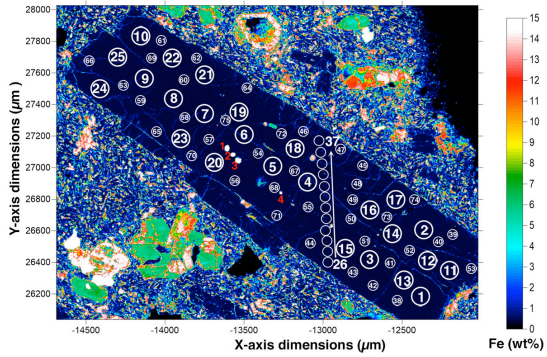

ALIA-115-18-2

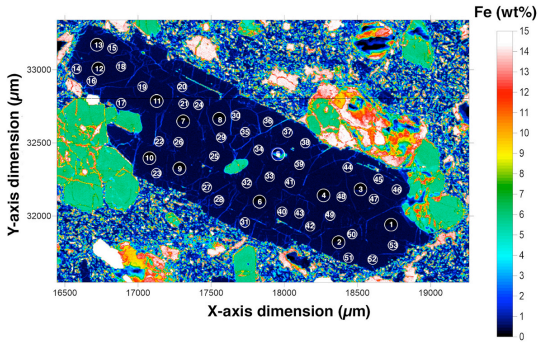

ALIA-115-18-3

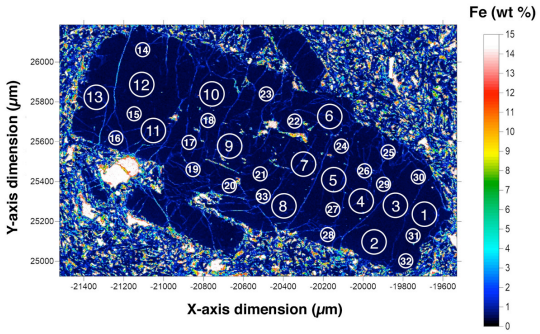

ALIA-115-21-1

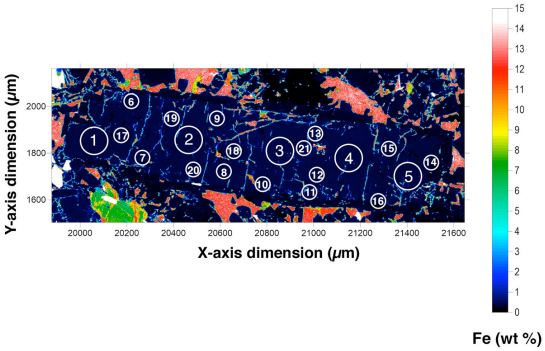

ALIA-115-21-2

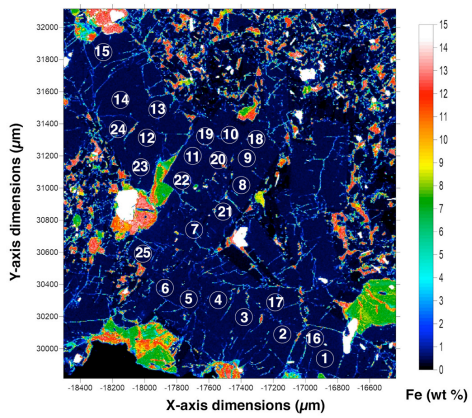

ALIA-115-21-3

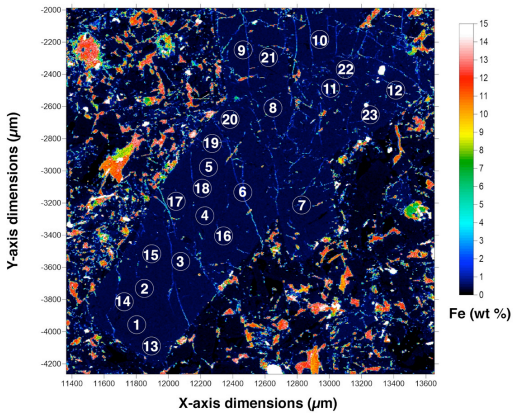

ALIA-115-18-1

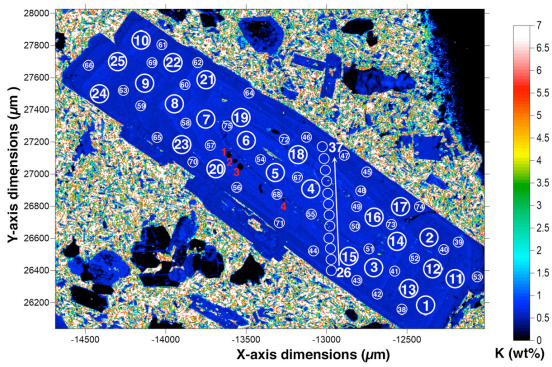

ALIA-115-18-2

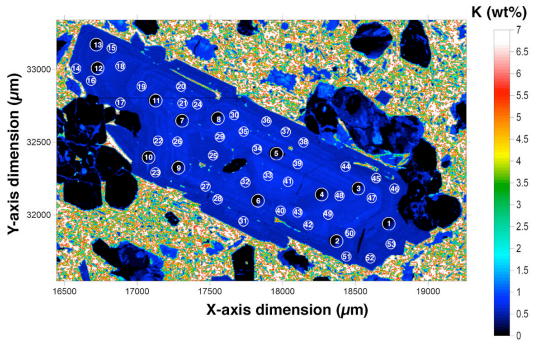

ALIA-115-18-3

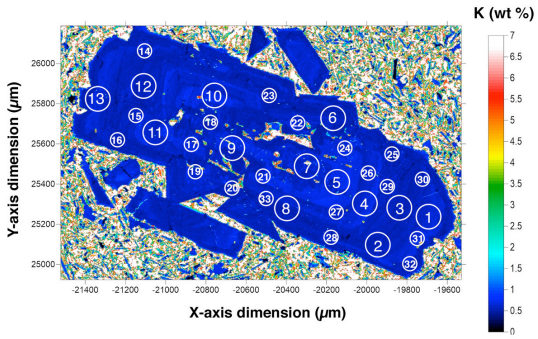

ALIA-115-21-1

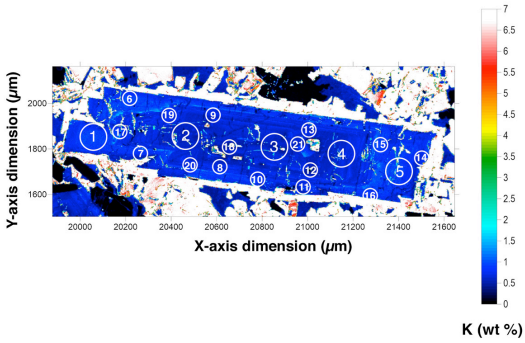

ALIA-115-21-2

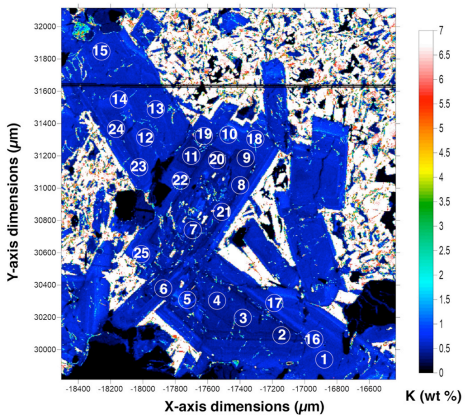

ALIA-115-21-3

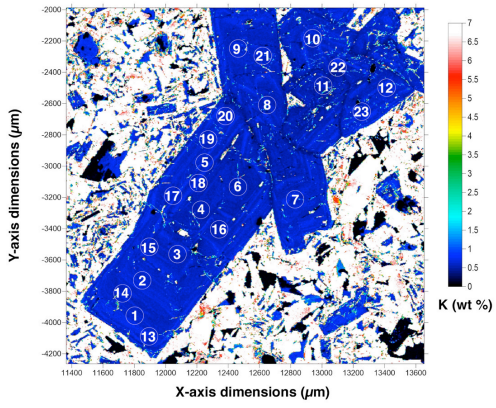

ALIA-115-18-1

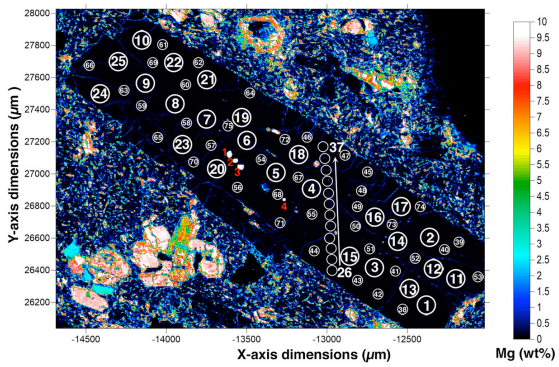

ALIA-115-18-2

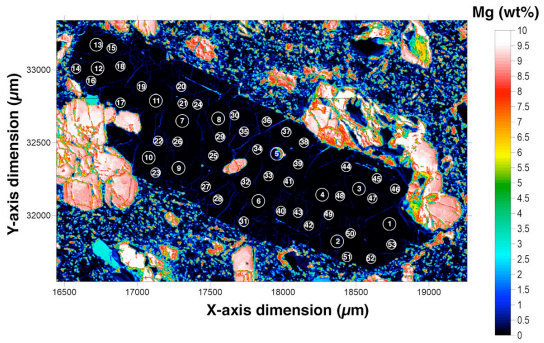

ALIA-115-18-3

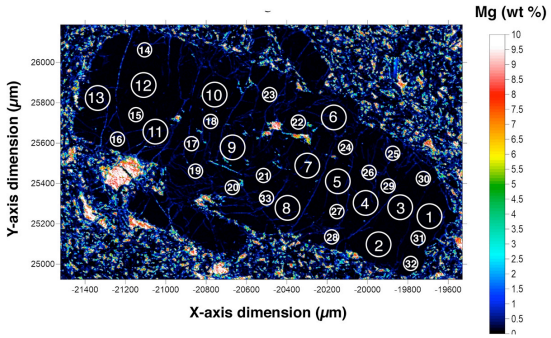

ALIA-115-21-1

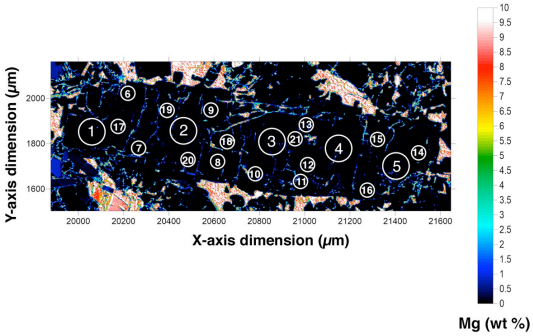

ALIA-115-21-2

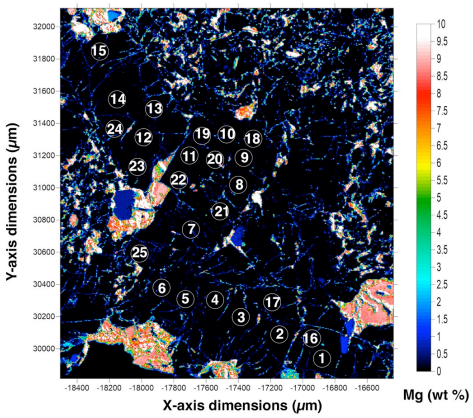

ALIA-115-21-3

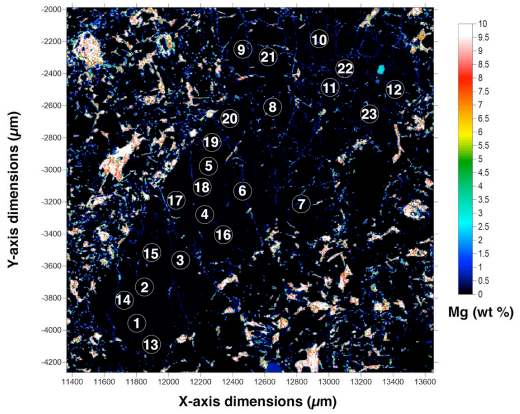

ALIA-115-18-1

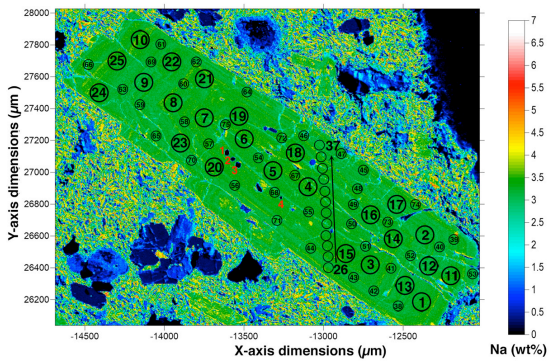

ALIA-115-18-2

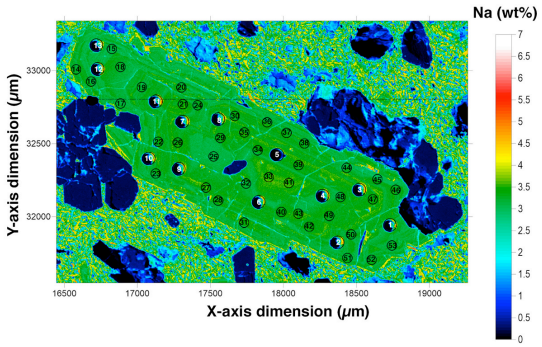

ALIA-115-18-3

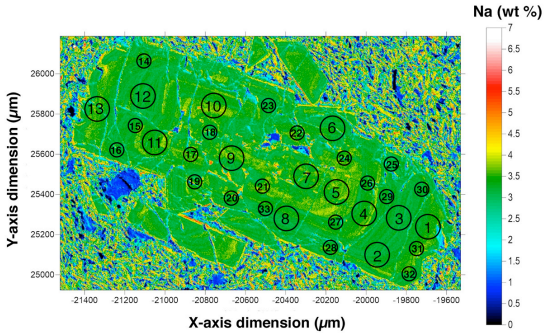

ALIA-115-21-1

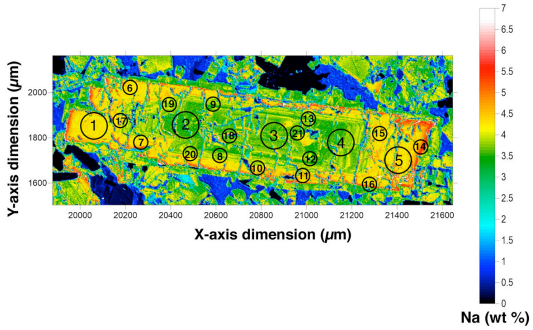

ALIA-115-21-2

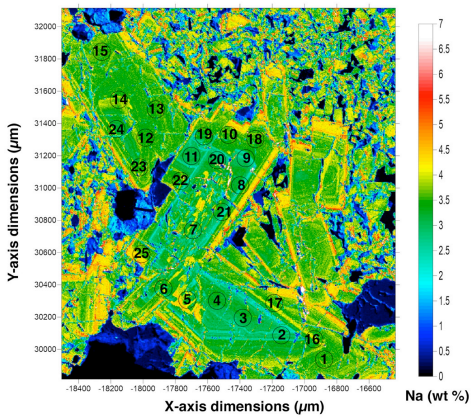

ALIA-115-21-3

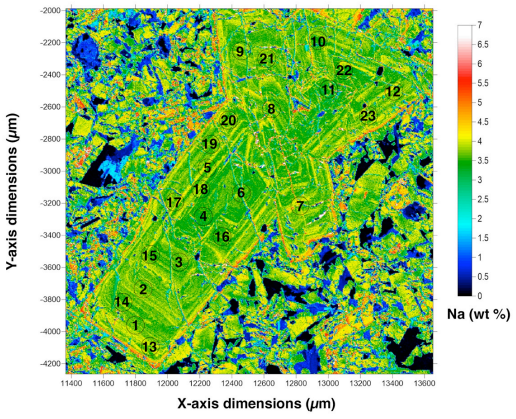

ALIA-115-18-1

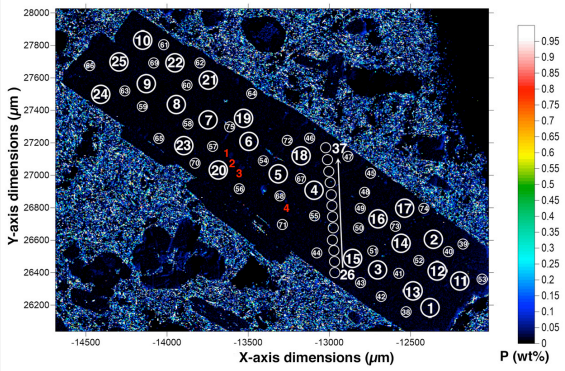

ALIA-115-18-2

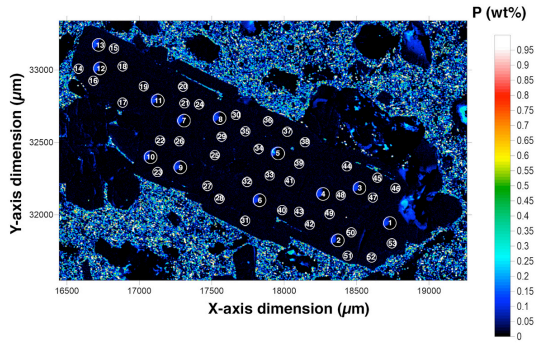

ALIA-115-18-3

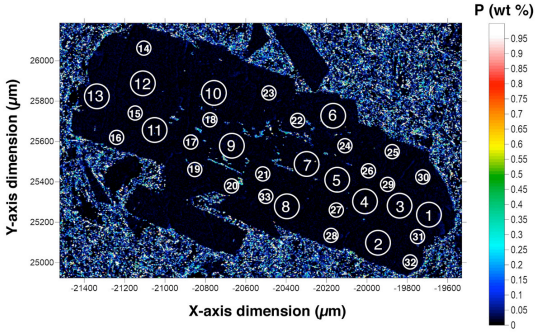

ALIA-115-21-1

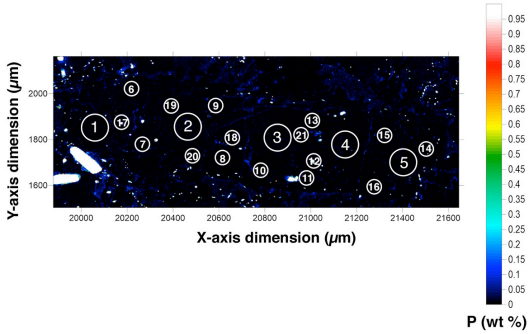

ALIA-115-21-2

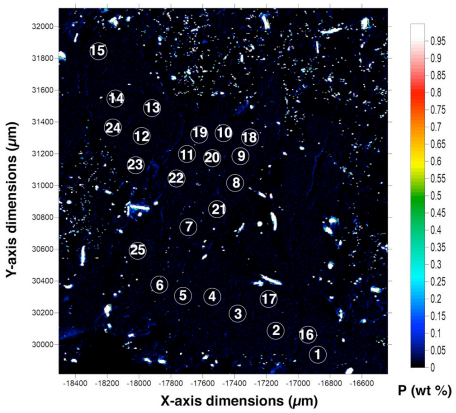

ALIA-115-21-3

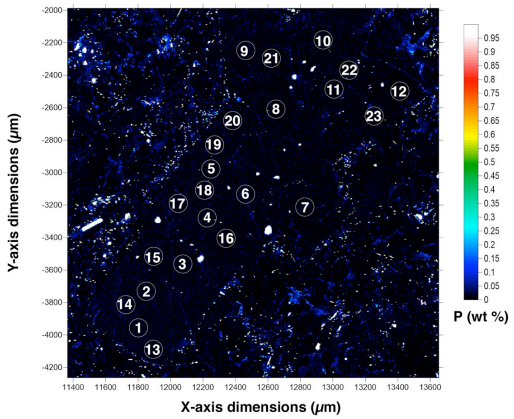

ALIA-115-18-1

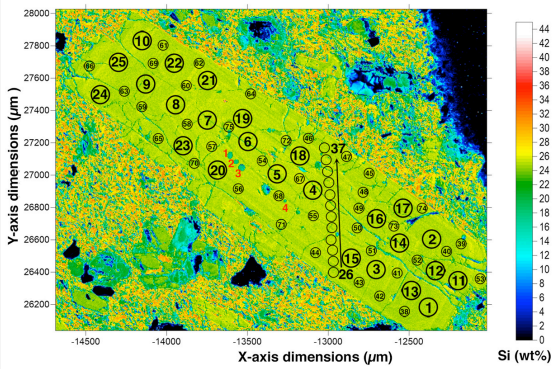

ALIA-115-18-2

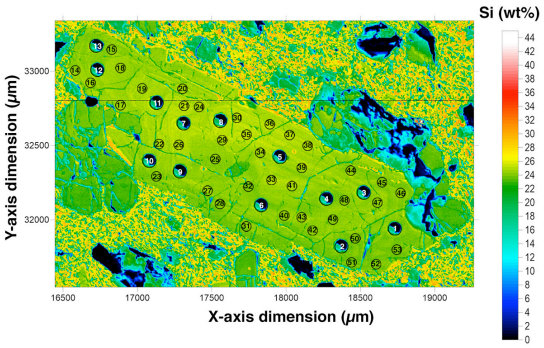

ALIA-115-18-3

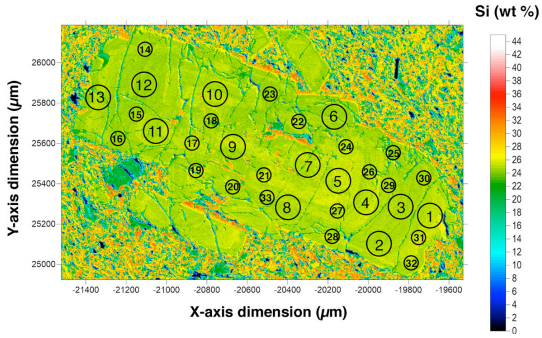

ALIA-115-21-1

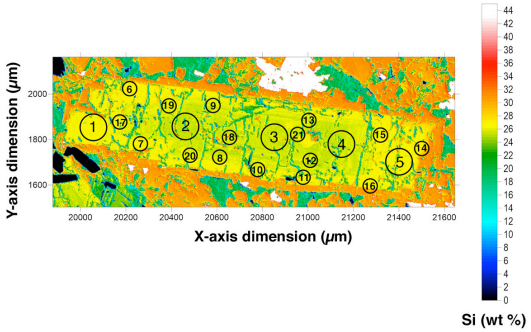

ALIA-115-21-2

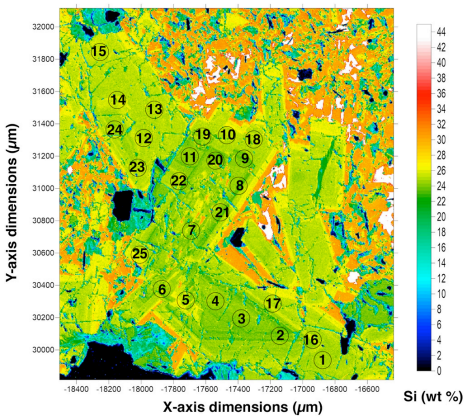

ALIA-115-21-3

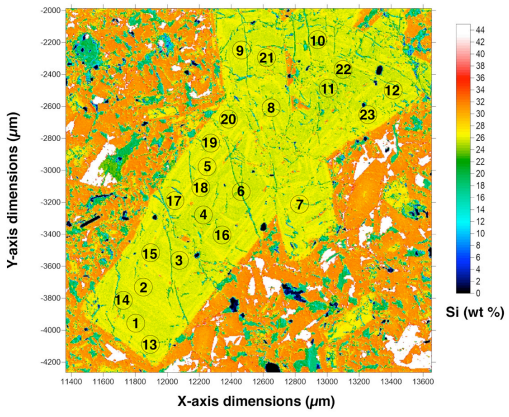

ALIA-115-18-1

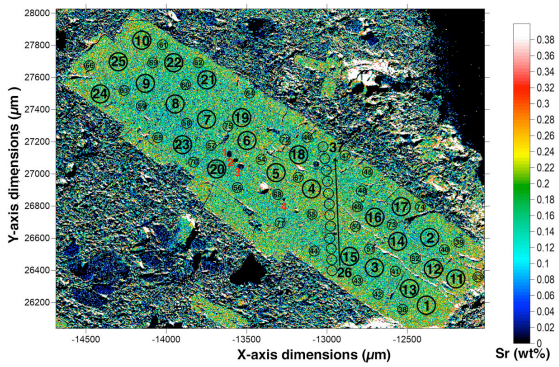

ALIA-115-18-2

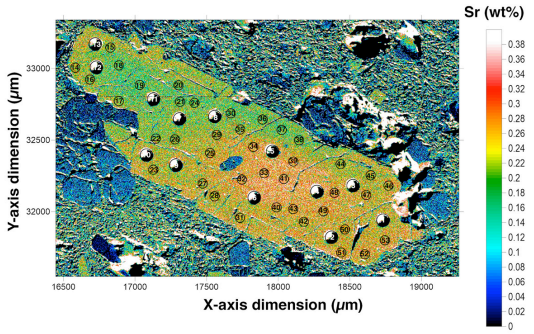

ALIA-115-18-3

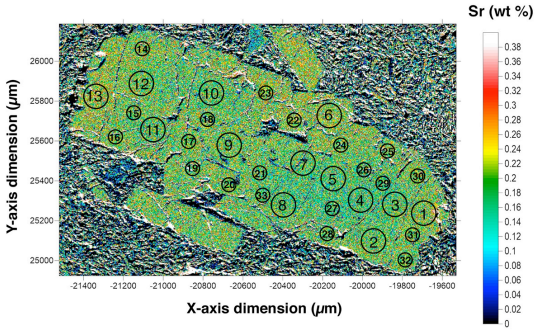

ALIA-115-21-1

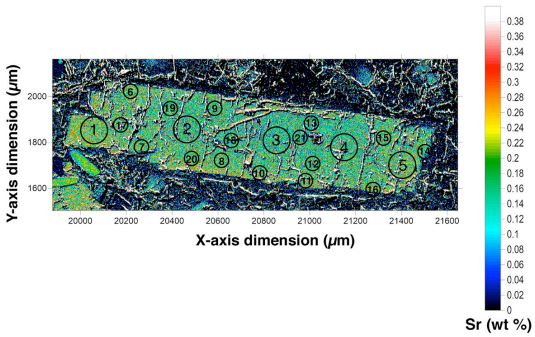

ALIA-115-21-2

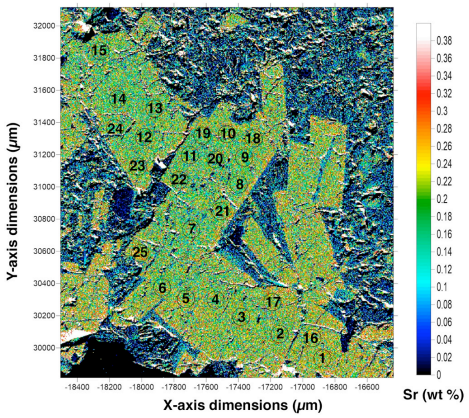

ALIA-115-21-3

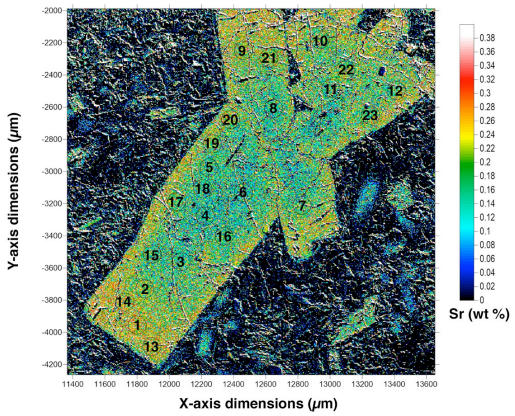

ALIA-115-18-1

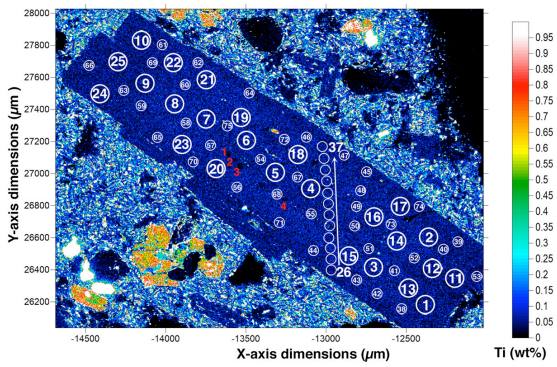

ALIA-115-18-2

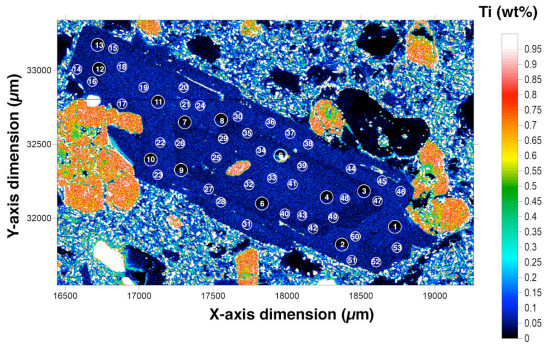

ALIA-115-18-3

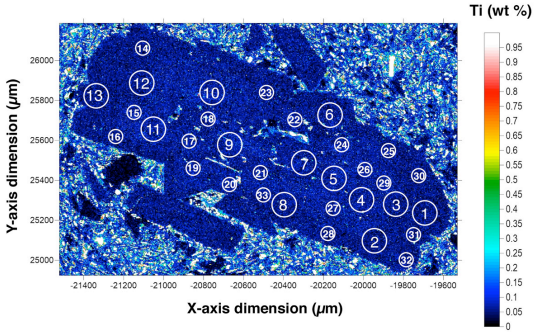

ALIA-115-21-1

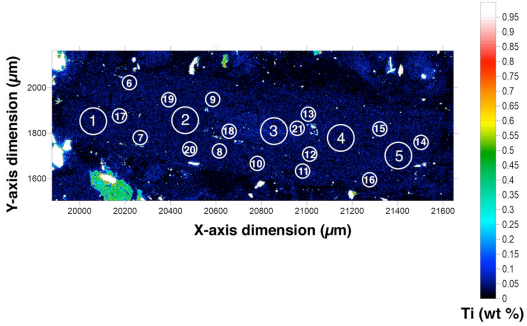

ALIA-115-21-2

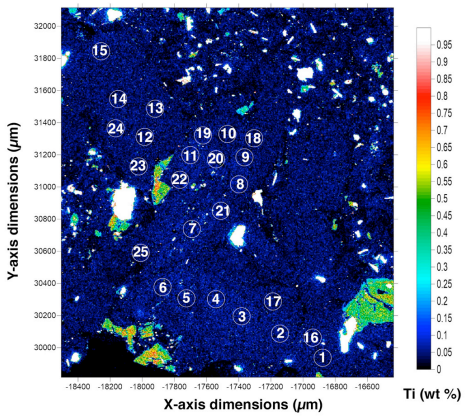

ALIA-115-21-3

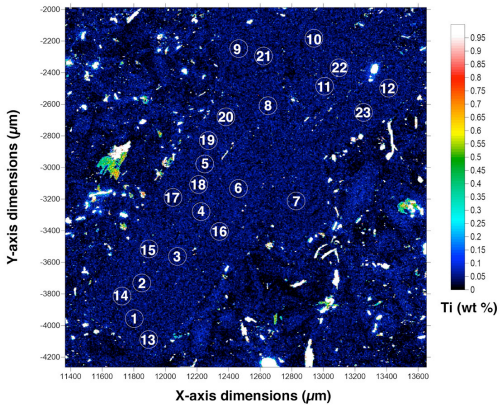

Supplementary Figure 1. Quantitative EPMA concentration maps of Al, Ca, Fe, K, Mg, Na, P, Si, Sr, and Ti for the six Samoan plagioclase crystals targeted in this study. All maps were generated via quantitative EPMA mapping using CalcImage (Probe Software, Inc.; see Supplementary Methods). The circles in each map correspond to laser spot locations and sizes, and the numbers correspond to the analysis number. We show the spot numbers of analyses that have been discarded for completeness. The geochemical data from each spot (including the average concentrations calculated from the EPMA maps, trace-element concentrations measured by LASS, and $^{87}Sr/^{86}Sr$ measured by LASS) are available in Supplementary Table 4.

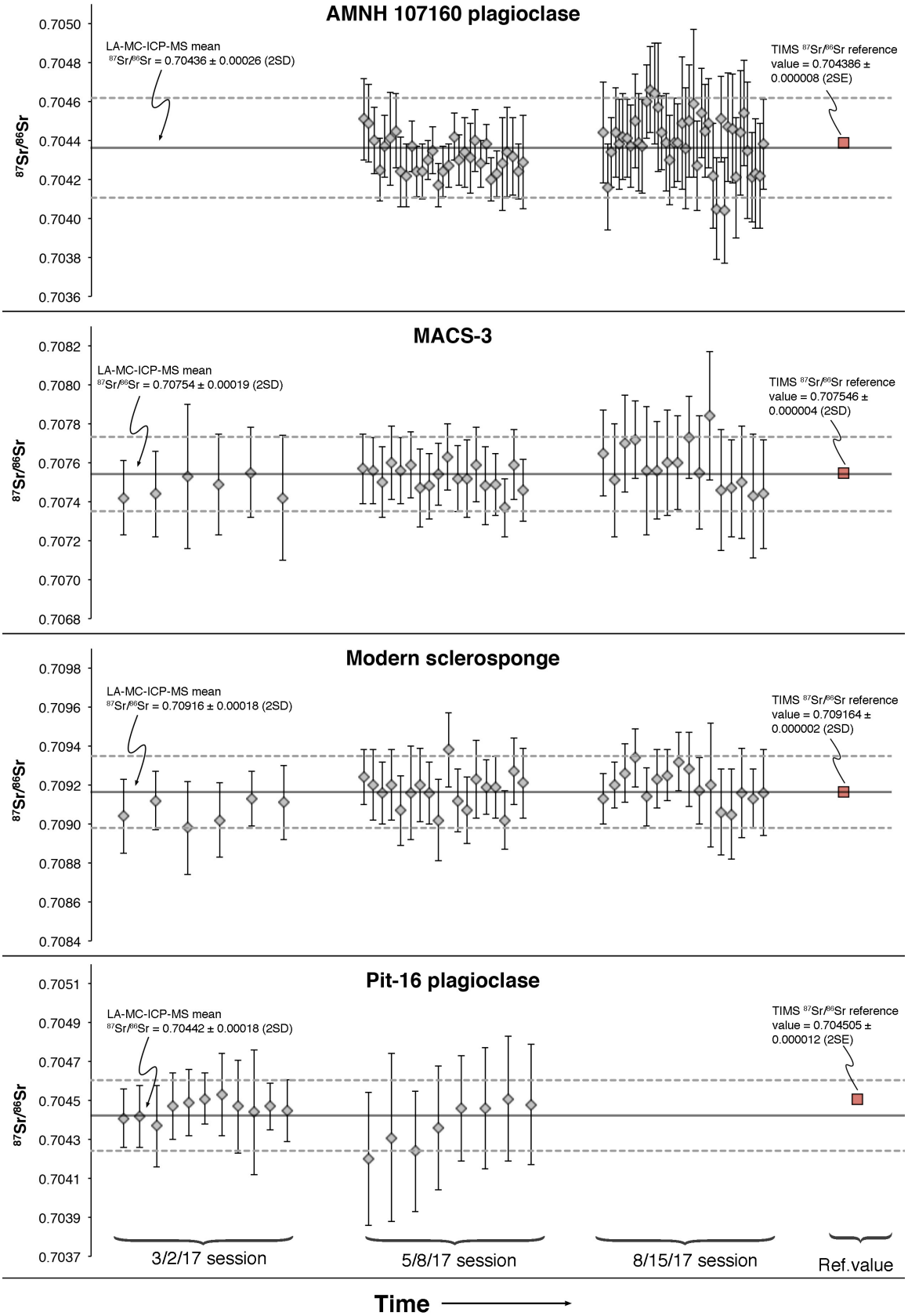
AMNH 107160 plagioclase
LA-MC-ICP-MS mean
87Sr/86Sr = 0.70436 ± 0.00026 (2SD)
TIMS 87Sr/86Sr reference value = 0.704386 ± 0.000008 (2SE)
87Sr/86Sr
0.7050
0.7048
0.7046
0.7044
0.7042
0.7040
0.7038
0.7036
MACS-3
LA-MC-ICP-MS mean
87Sr/86Sr = 0.70754 ± 0.00019 (2SD)
TIMS 87Sr/86Sr reference value = 0.707546 ± 0.000004 (2SD)
87Sr/86Sr
0.7082
0.7080
0.7078
0.7076
0.7074
0.7072
0.7070
0.7068
Modern sclerosponge
LA-MC-ICP-MS mean
87Sr/86Sr = 0.70916 ± 0.00018 (2SD)
TIMS 87Sr/86Sr reference value = 0.709164 ± 0.000002 (2SD)
87Sr/86Sr
0.7098
0.7096
0.7094
0.7092
0.7090
0.7088
0.7086
0.7084
Pit-16 plagioclase
LA-MC-ICP-MS mean
87Sr/86Sr = 0.70442 ± 0.00018 (2SD)
TIMS 87Sr/86Sr reference value = 0.704505 ± 0.000012 (2SE)
87Sr/86Sr
0.7051
0.7049
0.7047
0.7045
0.7043
0.7041
0.7039
0.7037
3/2/17 session
5/8/17 session
8/15/17 session
Ref.value
Time

Supplementary Figure 2. Measured (by LASS) $^{87}Sr/^{86}Sr$ of reference materials AMNH 107160, MACS-3, modern sclerosponge, and isotopically homogeneous plagioclase crystal Pit-16 (from Pitcairn Island; Garapić et al., 2015) over the course of this study. See Supplementary Table 3 for the reference material data used to make this figure. Analyses for each material are plotted in temporal order and are grouped by analytical session. The mean $^{87}Sr/^{86}Sr$ measured by LASS of each material is shown with a solid line, and the mean ± 2 SD is shown with a dashed line. Error bars for individual LASS analyses are internal 2 SE. The reference values for each material are shown with red squares. All reference values shown are corrected to NBS987 $^{87}Sr/^{86}Sr = 0.710240$. TIMS reference values for AMNH 107160 and Pit-16 are from this study and were measured on a mineral chip and a micromilled powder, respectively (see Table 2). Because the reference values for these materials consist of one measurement by TIMS, the reported uncertainties are 2 SE. The reference value for MACS-3 comes from Jochum et al. (2011), and the modern sclerosponge value—which we assume is identical to the Sr isotopic composition of modern seawater—is from Mokadem et al. (2015). These reference values consist of multiple measurements, and the uncertainties are 2 SD. The measured LASS and reference TIMS $^{87}Sr/^{86}Sr$ values for reference materials show excellent agreement.

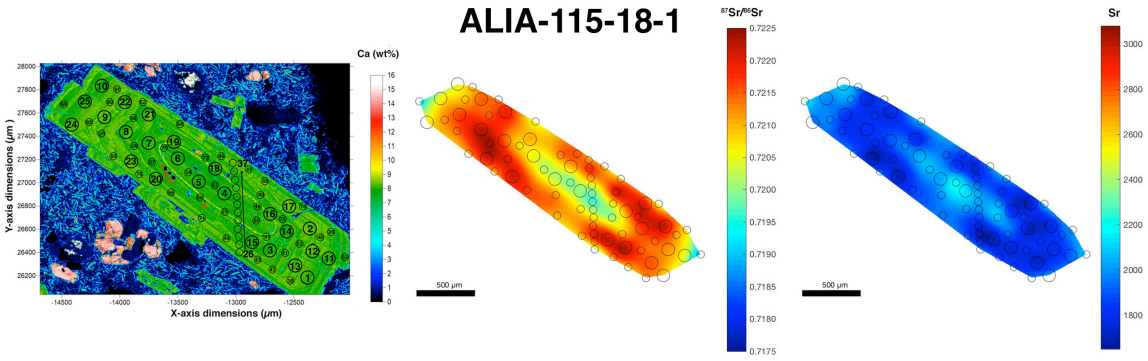
ALIA-115-18-1
Ca (wt%)
Y-axis dimensions (μm)
X-axis dimensions (μm)
87Sr/86Sr
Sr
500 μm

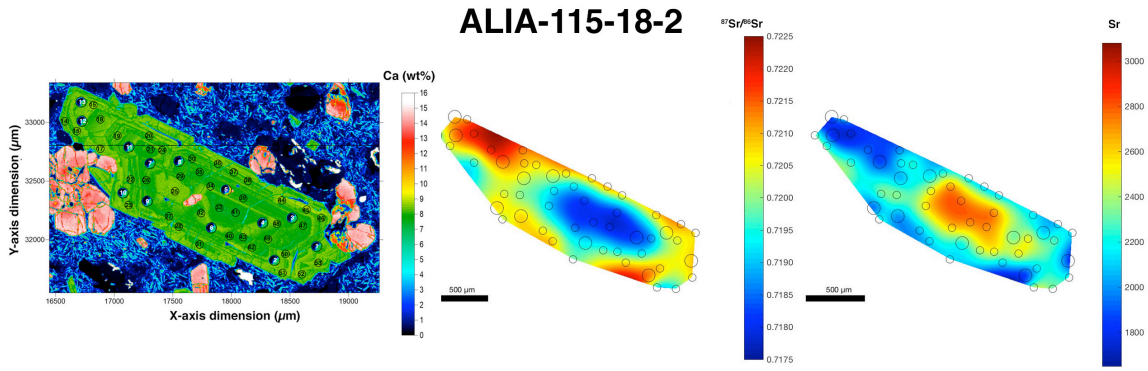
ALIA-115-18-2
Ca (wt%)
Y-axis dimension (μm)
X-axis dimension (μm)
87Sr/86Sr
Sr
500 μm

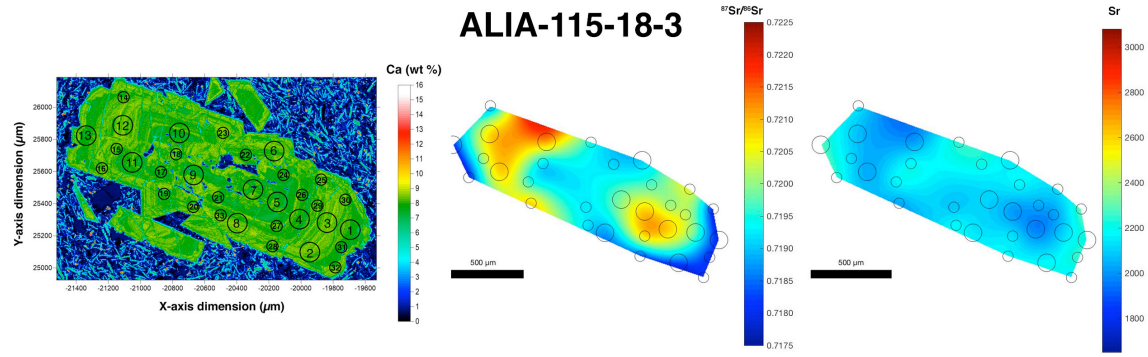
ALIA-115-18-3
Ca (wt %)
Y-axis dimension (μm)
X-axis dimension (μm)
87Sr/86Sr
Sr
500 μm

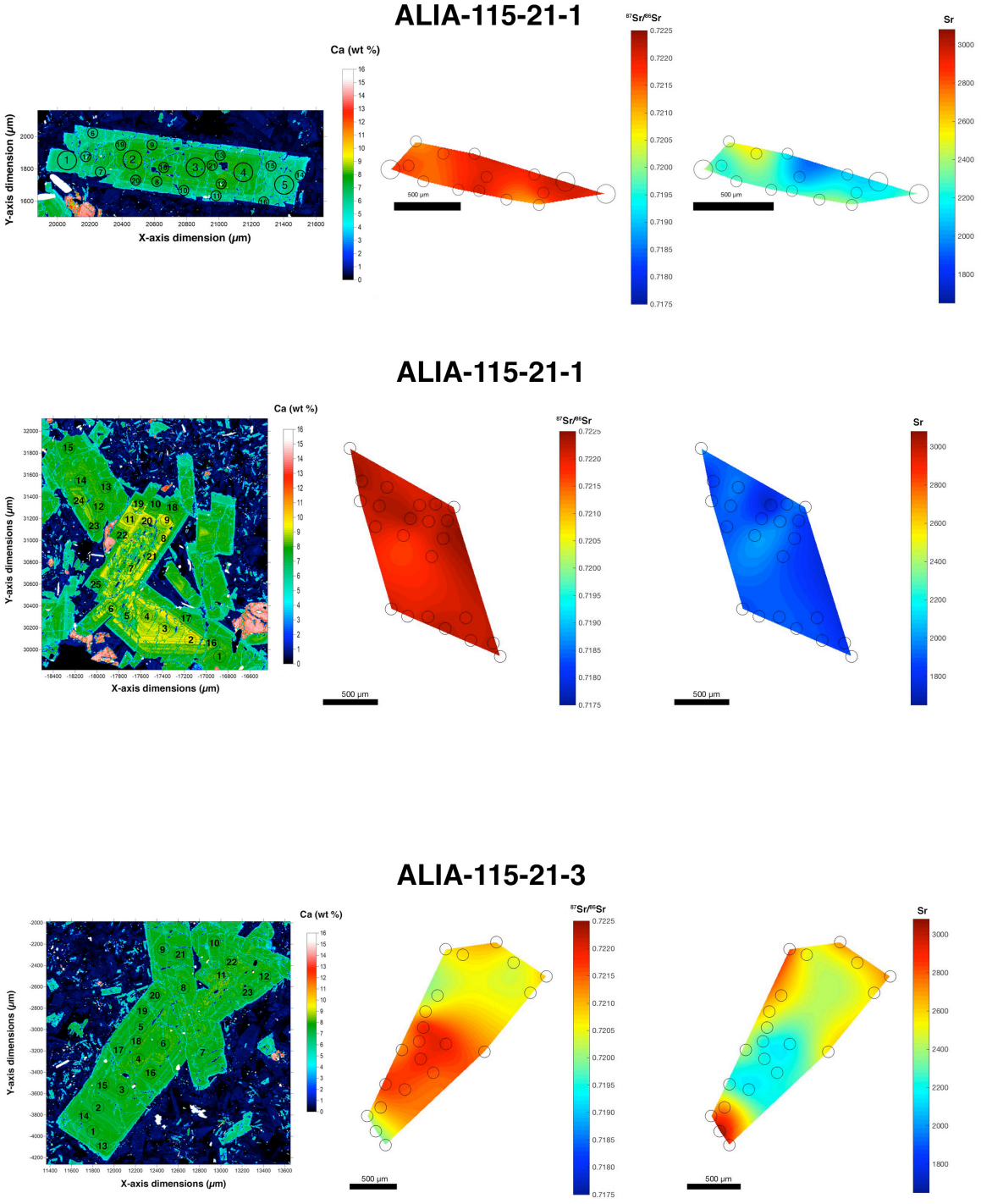

Supplementary Figure 3. Quantitative Ca concentration maps (left), $^{87}Sr/^{86}Sr$ model surfaces (middle), and Sr concentration model surfaces (right) for the six Samoan plagioclase crystals targeted in this study. The Ca EPMA maps were quantified using CalcImage (Probe Software, Inc). The $^{87}Sr/^{86}Sr$ and Sr concentration surfaces were generated using the 'gridfit' function in Matlab® (see Supplementary Methods). The

data used to construct the model surfaces are reported in Supplementary Table 4. The EPMA maps and model surfaces are scaled identically to enable comparisons between each panel. Similarly, the scales for Ca, $^{87}Sr/^{86}Sr$, and Sr are held constant for each crystal in order to facilitate comparisons between crystals. Therefore, a larger range in colors in a given Sr model surface corresponds to a greater range in measured $^{87}Sr/^{86}Sr$ or Sr concentration. The locations and diameters of the circles on each map correspond to locations and sizes of the laser spots. Each spot's number shown in the Ca map corresponds to the analysis number in Supplementary Table 4.

C. Tables

Table 1. Compositions of four olivines included in plagioclase ALIA-115-18-1.

	Number of spot analyses	SiO_2 (wt.%)	2σ	MgO (wt.%)	2σ	FeO (wt.%)	2σ	NiO (wt.%)	2σ	MnO (wt.%)	2σ	Al_2O_3 (wt.%)	2σ	Cr_2O_3 (wt.%)	2σ	CaO (wt.%)	2σ	Total (wt.%)	Fo#	2σ
Olivine 1	**5**	**37.76**	**0.42**	**37.38**	**0.40**	**22.98**	**0.12**	**0.11**	**0.01**	**0.31**	**0.01**	**0.02**	**0.01**	**0.01**	**0.02**	**0.28**	**0.02**	**98.86**	**74.36**	**0.27**
Olivine 2	**3**	**39.22**	**1.10**	**38.79**	**1.05**	**22.95**	**0.01**	**0.11**	**0.00**	**0.31**	**0.01**	**0.03**	**0.02**	**0.00**	**0.01**	**0.31**	**0.02**	**101.72**	**75.08**	**0.50**
Olivine 3	**5**	**37.68**	**0.25**	**37.15**	**0.29**	**23.07**	**0.09**	**0.11**	**0.01**	**0.31**	**0.01**	**0.03**	**0.01**	**0.01**	**0.01**	**0.28**	**0.01**	**98.63**	**74.17**	**0.12**
Olivine 4	**1**	**37.61**	**n/a**	**37.05**	**n/a**	**22.61**	**n/a**	**0.10**	**n/a**	**0.31**	**n/a**	**0.05**	**n/a**	**0.00**	**n/a**	**0.37**	**n/a**	**98.10**	**74.50**	**n/a**

Four olivines included in a zone in the ALIA-115-18-1 plagioclase crystal were analyzed by EPMA as described in the text. Each olivine was analyzed at between 1 to 5 separate spot locations. The 2 SD reproducibility of each oxide and of the calculated Fo# of olivines that were analyzed multiple times are reported.

Table 2. New TIMS analyses of reference materials in this study.

Sample name	Sample type	Estimated Sr (ng)[1]	TIMS $^{87}Sr/^{86}Sr$[2]	2 SE	LA-MC-ICP-MS $^{87}Sr/^{86}Sr$[3]	2 SD
Analyses conducted October 2015						
NBS987	Solution	-	0.710247	0.000015	-	-
BHVO-1	Powder	-	0.703503	0.000004	-	-
T21 homogenized plagioclase	Mineral fragment	-	0.704712	0.000009	-	-
Analyses conducted October 2017						
NBS987	Solution	-	0.710233	0.000014	-	-
BHVO-2	Powder	-	0.703470	0.000012	-	-
T21 homogenized plagioclase	Micromilled powder	18	0.704699	0.000018	-	-
AMNH 107160 plagioclase	Mineral fragment	-	0.704386	0.000008	0.70436	0.00026
AMNH 107160 plagiocalse	Micromilled powder	15	0.704408	0.000020	0.70436	0.00026
Pit-16 plagioclase	Micromilled powder	49	0.704505	0.000012	0.70442	0.00018

[1]Sr quantities for micromilled powders are estimated from the milled volume and the measured Sr concentration of each plagioclase (see Supplementary Table 2), and assume 100% recovery and a plagioclase density of 2.7 g/cm^3.

[2]Aside from NBS987, all reported $^{87}Sr/^{86}Sr$ values are normalized to NBS987 $^{87}Sr/^{86}Sr$ = 0.710240.

[3]LA-MC-ICP-MS values are averages of multiple analyses over the course of this study, which are summariezd in Table 3 and reported in Supplementary Table 3.

Table 3. $^{87}Sr/^{86}Sr$ values measured from geological reference materials by LA-MC-ICP-MS in this study compared to TIMS reference values.

Reference material	$^{87}Sr/^{86}Sr$ by LA-MC-ICP-MS [1]	LA-MC-ICP-MS 2SD	LA-MC-ICP-MS 2SD (ppm)	Number of analyses	TIMS reference $^{87}Sr/^{86}Sr$ [2]	TIMS reference uncertainty[3]	Difference between LA-MC-ICP-MS and TIMS reference values (ppm)
AMNH 107160 plagioclase	0.70436	0.00026	363	73	0.704386	0.000008 (2SE)	-33
Pit-16 plagioclase	0.70442	0.00018	257	19	0.704505	0.000012 (2SE)	-115
USGS MACS-3 carbonate	0.70754	0.00019	270	40	0.707546	0.000004 (2SD, n=5)	-6
Modern sclerosponge	0.70916	0.00018	260	40	0.709164	0.000002 (2SD, n=17)	1

[1]Refer to Supplementary Table 3 for the individual analyses used to calculate the mean measured Sr isotopic composition and uncertainties reported here.

[2]The reference values for AMNH 107160 plagioclase and Pit-16 plagioclase were obtained by TIMS and are reported in Table 2. The USGS MACS-3 carbonate reference value is reported in Jochum et al. (2011). The reference value for the modern sclerosponge is the modern seawater value of Mokadem et al. (2015). All reference and measured values have been normalized to NBS987 $^{87}Sr/^{86}Sr$=0.710240.

[3]Reference value analytical uncertainties for AMNH 107160 and Pit-16 plagioclase are 2 SE. Uncertainties for MACS-3 and modern sclerosponge—for which reference values are means of multiple ratios—are 2 SD.

Supplementary Table 1. EPMA analyses of plagioclase reference materials used in this study.

Sample name	SiO_2	Al_2O_3	Na_2O	MgO	FeO	TiO_2	SrO	P_2O_5	K_2O	CaO	Total
T21 plagioclase	58.19	26.58	4.01	0.12	0.52	0.17	0.15	0.03	0.64	9.85	100.27
T21 plagioclase	58.20	26.54	3.93	0.12	0.55	0.18	0.16	0.04	0.66	9.87	100.24
T21 plagioclase	58.12	26.53	3.93	0.12	0.52	0.20	0.16	0.03	0.63	9.87	100.11
T21 plagioclase	58.13	26.61	4.00	0.13	0.54	0.18	0.15	0.02	0.61	9.85	100.23
T21 plagioclase	58.06	26.49	3.98	0.11	0.52	0.16	0.17	0.03	0.67	9.89	100.09
T21 plagioclase	58.16	26.48	4.06	0.12	0.57	0.19	0.17	0.04	0.67	9.85	100.31
T21 plagioclase	58.21	26.42	3.99	0.11	0.53	0.19	0.15	0.03	0.62	9.78	100.03
T21 plagioclase	58.07	26.40	4.03	0.11	0.54	0.20	0.13	0.03	0.62	9.80	99.92
T21 plagioclase	58.23	26.54	3.97	0.14	0.52	0.17	0.16	0.04	0.64	9.86	100.27
T21 plagioclase	58.08	26.60	3.99	0.12	0.55	0.20	0.14	0.02	0.63	9.86	100.18
Average	*58.14*	*26.52*	*3.99*	*0.12*	*0.54*	*0.19*	*0.15*	*0.03*	*0.64*	*9.85*	*100.16*
2 SD	*0.13*	*0.14*	*0.08*	*0.02*	*0.03*	*0.03*	*0.03*	*0.02*	*0.04*	*0.07*	*0.25*
AMNH plagioclase chip 1	52.92	30.66	4.41	0.10	0.33	0.02	0.08	0.00	0.26	12.09	100.87
AMNH plagioclase chip 1	52.82	30.50	4.46	0.10	0.35	0.06	0.11	0.00	0.27	11.94	100.60
AMNH plagioclase chip 1	52.55	30.72	4.41	0.11	0.33	0.07	0.15	0.01	0.27	12.14	100.75
AMNH plagioclase chip 1	52.67	30.70	4.41	0.11	0.38	0.06	0.12	-	0.26	12.07	100.78
AMNH plagioclase chip 1	52.62	30.68	4.46	0.12	0.35	0.07	0.10	0.01	0.26	12.06	100.73
AMNH plagioclase chip 1	52.89	30.61	4.45	0.10	0.35	0.08	0.08	0.00	0.27	12.09	100.93
AMNH plagioclase chip 1	52.45	30.60	4.41	0.11	0.33	0.06	0.13	0.01	0.26	12.13	100.49
AMNH plagioclase chip 1	52.68	30.53	4.47	0.10	0.31	0.05	0.15	0.00	0.28	12.04	100.59
AMNH plagioclase chip 1	52.51	30.55	4.42	0.11	0.33	0.07	0.12	0.00	0.27	12.08	100.46
AMNH plagioclase chip 1	52.68	30.52	4.46	0.12	0.32	0.06	0.14	0.01	0.27	12.11	100.69
AMNH plagioclase chip 2	52.95	30.58	4.52	0.12	0.36	0.07	0.08	0.01	0.28	11.97	100.92
AMNH plagioclase chip 2	53.02	30.52	4.48	0.11	0.32	0.05	0.12	0.01	0.27	12.01	100.93
AMNH plagioclase chip 2	52.91	30.59	4.53	0.11	0.33	0.07	0.14	0.00	0.27	11.97	100.91
AMNH plagioclase chip 2	52.84	30.46	4.50	0.11	0.34	0.04	0.12	0.01	0.29	12.02	100.73
AMNH plagioclase chip 2	53.01	30.79	4.50	0.12	0.31	0.04	0.10	0.01	0.27	12.07	101.21
AMNH plagioclase chip 2	52.73	30.51	4.50	0.11	0.35	0.06	0.13	0.00	0.29	12.03	100.70
AMNH plagioclase chip 2	52.94	30.40	4.51	0.11	0.36	0.06	0.09	0.01	0.27	12.06	100.80
AMNH plagioclase chip 2	52.93	30.54	4.46	0.11	0.36	0.03	0.13	-	0.26	12.03	100.84
AMNH plagioclase chip 2	52.88	30.48	4.50	0.12	0.35	0.07	0.10	-	0.28	12.05	100.83
AMNH plagioclase chip 2	52.80	30.50	4.53	0.10	0.34	0.05	0.11	0.00	0.27	11.94	100.64
Average	*52.79*	*30.57*	*4.47*	*0.11*	*0.34*	*0.06*	*0.11*	*0.00*	*0.27*	*12.05*	*100.77*
2 SD	*0.34*	*0.19*	*0.08*	*0.01*	*0.04*	*0.03*	*0.05*	*0.02*	*0.02*	*0.12*	*0.35*

T21 concentrations reported here are from a single chip. AMNH concentrations reported here are from two chips that show good agreement in terms of their major-element compositions.

Supplementary Table 2. Summary of reference material major-element and trace-element concentrations measured by LA-Q-ICP-MS in this study

Element	KL2-G measured concentration	2 SD	2 SD (%)	KL2-G reference value[1]	Uncertainty[2]	Difference from reference value (%)	ML3B-G measured concentration	2 SD	2 SD (%)	ML3B-G reference value[1]	Uncertainty[2]	Difference from reference value (%)	T21 homogenized plagioclase measured concentration	2 SD	2 SD (%)	T21 homogenized plagioclase reference value[3,4]	2 SD	Difference from reference value (%)	AMNH 107160 plagioclase measured concentration[5]	2 SD	2 SD (%)
Na (wt%)	1.83	0.09	4.7	1.74	0.06	4.8	1.92	0.13	6.8	1.78	0.04	7.7	2.77	0.24	8.6	2.96	0.06	-6.3	3.15	0.16	5.1
Al (wt%)	7.02	0.14	2.0	7.04	0.11	-0.3	7.34	0.21	2.9	7.20	0.11	2.0	13.2	0.42	3.2	14.0	0.1	-6.1	15.3	0.48	3.2
Si (wt%)	23.1	0.7	3.1	23.5	0.14	-1.7	24.2	1.1	4.4	24.0	0.3	0.8	25.0	1.5	6.0	27.2	0.1	-8.0	23.0	1.0	4.3
K (wt%)	0.40	0.02	4.0	0.40	0.01	1.3	0.33	0.02	5.8	0.320	0.003	2.0	0.44	0.04	8.7	0.5	0.03	-16.2	0.20	0.01	5.0
Ti (wt%)	1.56	0.026	1.6	1.53	0.054	1.4	1.29	0.026	2.1	1.28	0.05	0.7	0.12	0.006	4.9	0.11	0.02	6.2	0.04	0.002	6.4
Fe (wt%)	8.45	0.28	3.3	8.32	0.08	1.6	8.83	0.29	3.3	8.47	0.08	4.3	0.42	0.02	5.0	0.42	0.03	-0.2	0.26	0.01	3.5
Rb (ppm)	8.64	0.41	4.7	8.70	0.40	-0.6	5.98	0.32	5.4	5.80	0.21	3.0	13.70	4.26	31.1	20.67	4.95	-33.7	0.35	0.07	19.8
Sr (ppm)	358	7.2	2.0	356	8.0	0.7	317	7.2	2.3	312	4	1.6	1306	124	9.5	1346	154	-3.0	968	89	9.2
Y (ppm)	26.6	0.7	2.7	25.4	1.1	4.6	25.3	0.9	3.5	23.9	0.7	5.8	1.34	0.13	9.4	1.25	0.12	6.6	0.29	0.04	12.8
Ba (ppm)	122.5	4.2	3.4	123.0	5.0	-0.4	81.1	2.6	3.2	80.1	2.2	1.2	206.0	14.9	7.2	204.6	9.0	0.7	118.0	5.6	4.8
La (ppm)	13.28	0.41	3.1	13.1	0.20	1.4	9.09	0.35	3.9	8.99	0.13	1.1	5.43	0.63	11.7	5.07	0.49	7.0	1.31	0.11	8.5
Ce (ppm)	32.81	1.01	3.1	32.4	0.70	1.3	23.52	0.82	3.5	23.10	0.30	1.8	8.84	0.72	8.2	8.36	0.98	5.7	2.33	0.15	6.4
Pr (ppm)	4.73	0.16	3.4	4.60	0.10	2.8	3.52	0.13	3.8	3.43	0.06	2.5	0.93	0.10	10	0.85	0.04	8.9	0.27	0.03	11.5
Nd (ppm)	21.76	1.03	4.7	21.6	0.40	0.7	17.11	0.56	3.3	16.70	0.20	2.5	3.32	0.30	9.1	3.14	0.26	6.0	1.04	0.11	10.7
Sm (ppm)	5.65	0.36	6.3	5.54	0.09	1.9	4.75	0.35	7.4	4.75	0.07	0.1	0.49	0.09	18	0.46	0.07	7.0	0.16	0.05	33.3
Eu (ppm)	1.96	0.08	4.0	1.92	0.04	2.0	1.73	0.13	7.3	1.67	0.02	3.9	1.64	0.13	7.7	1.56	0.20	5.3	0.42	0.04	10.1
Gd (ppm)	6.01	0.44	7.4	5.92	0.20	1.5	5.33	0.28	5.2	5.26	0.23	1.4	0.37	0.07	18	0.42	0.06	-10.7	0.12	0.05	43.0
Er (ppm)	2.66	0.17	6.5	2.54	0.07	4.5	2.58	0.21	8.2	2.44	0.05	5.6	0.13	0.03	24	0.12	0.002	4.7	0.02	0.02	105
Yb (ppm)	2.10	0.12	5.8	2.10	0.05	0.01	2.08	0.14	6.7	2.06	0.04	0.9	0.12	0.04	35	0.12	0.01	2.1	0.01	0.03	259
Lu (ppm)	0.29	0.03	10.1	0.29	0.01	2.7	0.29	0.03	11.4	0.29	0.01	1.9	0.02	0.01	50	0.02	0.01	-12.8	0.001	0.01	557

The reference material measurements reported here represent multiple analyses of each sample: KL2-G (n=26), ML3B-G (n=26), T21 (n=95), AMNH (n=73). The 2 SD errors for the new data reflect the variability over multiple analyses. Refer to Supplementary Table 3 for the individual analyses used to calculate the mean elemental concentrations and the uncertainties reported in this table.

[1]Reference values for KL2-G and ML3-B are from Jochum et al. (2006).

[2]95% confidence interval. Uncertainties are from Jochum et al. (2006).

[3]Major-element reference values for T21 homogenized plagioclase are by EPMA. and are reported in wt%. See Supplementary Table 1 for the EPMA analyses.

[4]Trace-element reference values for T21 plagioclase are from solution ICP-MS. where trace-element concentrations are reported in ppm.

[5]Solution-based ICP-MS trace-element concentrations for the AMNH 107160 plagioclase are not yet available. Nonetheless, we report AMNH 107160 plagioclase trace-element concentrations measured in this study by LA-Q-ICP-MS for completeness.

Supplementary Table 5. Nu *Plasma* detector configuration used in this study.

Detector	**AX**	**L1**	**L2**	**L3**	**L4**	**L5**	**L6**	**L7**	**L8**	**IC0**	**IC1**	**IC2**
Monitored mass	88	87.5	87	86.5	86	85.5	85	84.5	84	83	82.5	82

*AX = axial Faraday cup. L1–L8 are Faraday cups. IC0–IC2 are ion counters.